nuclear fusion
IAEA

PAPER • OPEN ACCESS

Multi-X-point radiation and its dynamics in up/down asymmetry in plasma detachment regimes in Wendelstein 7-X

To cite this article: D. Zhang *et al* 2025 *Nucl. Fusion* **65** 096032

OPEN ACCESS
IOP Publishing | International Atomic Energy Agency
Nuclear Fusion
Nucl. Fusion **65** (2025) 096032 (24pp)
https://doi.org/10.1088/1741-4326/adfc7d

Multi-X-point radiation and its dynamics in up/down asymmetry in plasma detachment regimes in Wendelstein 7-X

D. Zhang[1,*], G. Cseh[2], Y. Feng[1], Y. Gao[1], M. Jakubowski[1], T. Kremeyer[1], S. Dräger[1], F. Reimold[1], D.M. Kriete[3], A. Pandey[1], G. Schlisio[1], G. Partesotti[1], V. Perseo[1], A. Alonso[4], Ch. Biedermann[1], S.A. Bozhenkov[1], Ch. Brandt[1], K.J. Brunner[1], R. Burhenn[1], B. Buttenschön[1], M. Endler[1], G. Fuchert[1], J. Geiger[1], L. Giannone[5], V. Haak[1], K.C. Hammond[6], M. Hirsch[1], J. Knauer[1], G. Kocsis[2], M. Krychowiak[1], R. König[1], R. Laube[1], D. Naujoks[1], M. Otte[1], F. Penzel[7], E. Pasch[1], K. Rahbarnia[1], T. Szepesi[2], H. Thomsen[1], U. Wenzel[1], V. Winters[1] and the W7-X Team[a]

[1] Max-Planck-Institut für Plasmaphysik, D-17491 Greifswald, Germany
[2] HUN-REN Centre for Energy Research, Konkoly-Thege út 29-33, 1121 Budapest, Hungary
[3] Auburn University, Auburn, AL, United States of America
[4] Laboratorio Nacional de Fusión. CIEMAT, 28040 Madrid, Spain
[5] Max-Planck-Institut für Plasmaphysik, Garching, Germany
[6] Princeton Plasma Physics Laboratory, Princeton, NJ, United States of America
[7] ITER Organization, CS 90 046, 13067 St. Paul Lez Durance Cedex, France

E-mail: daihong.zhang@ipp.mpg.de

Received 2 June 2025, revised 5 August 2025
Accepted for publication 17 August 2025
Published 29 August 2025

Abstract

In Wendelstein 7-X (W7-X), stable plasma detachment in ECRH hydrogen plasmas is routinely achieved with the standard magnetic configuration, containing five magnetic islands in the scrape-off layer (SOL). Plasma detachment induced by intrinsic carbon impurities is characterized by a high radiation fraction (f_{rad}) with significantly reduced divertor heat load and particle flux. In this work, we present the radiation dynamics during the detached plasma (DP) phase, such as the shift of radiation zones in radial and poloidal directions towards the X-points as f_{rad} increases (∼0.6–0.9), as well as the penetration of the radiation layer into the confinement region in the deep DP phase with f_{rad} approaching unity. In particular, a structure of multi-X-point radiation (multi-XPR) with an up/down asymmetry in the DP phase is highlighted, which is revealed by bolometer tomography and is further confirmed by video diagnostics. The multi-XPR structure forms helical 3D bands aligned with W7-X field periodicity. Field reversal experiments show that the brightest XPR displaces between the upper

[a] See Grulke *et al* 2024 (https://doi.org/10.1088/1741-4326/ad2f4d) for the W7-X Team.
[*] Author to whom any correspondence should be addressed.

and lower SOL regions, suggesting the $\mathbf{E} \times \mathbf{B}$ drift effects. This paper presents the multi-XPR structure observed in the W7-X plasma in detail for the first time. A simplified model considering the influence of the poloidal $\mathbf{E} \times \mathbf{B}$ drift (V_d) on the impurity flow in the SOL shows that the downstream drift toward the target or target shadow region ($V_\mathrm{d} < 0$) decreases the impurity content, while the upstream drift toward the LCFS ($V_\mathrm{d} > 0$) increases the impurity content. On this basis, the poloidal drift potentially leads to an up/down asymmetry of impurity density in the SOL despite the symmetry magnetic topology. The dynamics of the up/down asymmetry in the multi-XPR structure is also related to the magnitude V_d/D (normalized to the impurity diffusivity), with an additional effect owing to the radial inward shift of the emission zone. These results provide new insights into impurity-induced detachment dynamics and provide a basis for improving 3D modeling of impurity transport, which typically does not consider drifts.

Keywords: X-point radiation, plasma detachment, W7-X, up/down asymmetry, $E \times B$ drift, impurity radiation, bolometer tomography

(Some figures may appear in colour only in the online journal)

1. Introduction

In magnetically confined fusion experiments, both tokamaks and stellarators face the critical challenge of mitigating heat fluxes on plasma-facing components (PFCs) to technically feasible levels. One promising solution is plasma detachment, which is characterized by high radiation loss. This research topic at tokamaks dates back several decades [1–5], while the related research on stellarators started another decade later [6–9] and has recently been studied in detail using the EMC3-Eirene code [10].

In tokamaks with carbon walls, high-radiation phases often exhibits plasma instabilities, such as MARFEs [11, 12], whereas in metal-wall experiments, stable and controllable detachment regimes can be established through impurity seeding—injections of low-to-medium Z impurities (such as N_2, Ne and Ar) [13–15]. In single-null configurations, an intense radiation zone called the X-point radiator (XPR) forms within the separatrix near the X-point, typically in cold and dense plasma regions [16–18].

In stellarator/heliotron devices such as the advanced stellarator Wendelstein 7-AS (W7-AS) [19] and the large helical device (LHD) [20], efforts were made to achieve stable plasma detachment. In W7-AS, where the island divertor concept was tested for the first time, stable detachment with significantly high impurity radiation could only be achieved partially [21] and was limited to certain configuration settings (adding external resonant magnetic perturbation fields (RMPs) by means of so-called island control coils). Attempts to achieve complete detachment at higher radiation levels led to thermal instabilities [22–24]. Similarly, in the helical divertor of the LHD, stable detachment is achieved by introducing an external 1/1 RMP field component [9]. Asymmetries in plasma radiation were generally observed in both devices, e.g. a pronounced in-out asymmetry in W7-AS, which was concentrated on the X-points on the inboard side [8, 23], while stronger radiation around the X-point of the 1/1 island in the LHD exhibits an up-down asymmetry at the upper and lower edges [25, 26].

The optimized quasi-isodynamic stellarator Wendelstein 7-X (W7-X) [27] also uses the island divertor concept [28], in which intrinsic magnetic islands (intersected by carbon target plates) form a 3D scrape-off layer (SOL). Already in its first divertor operational phase [29–31], stable plasma detachment in the standard magnetic configuration (SDC) has been routinely achieved, which is primarily caused by intrinsic impurities (such as carbon and oxygen) released from the PFCs. Before wall boronization (2017, OP1.2a), detachment was mainly driven by oxygen radiation [32]. In contrast, after boronization (2018, OP1.2b) [33, 34], carbon became the dominant radiator, increasing the critical density for high-radiation scenarios by a factor of $\sim$3 due to reduced oxygen [35]. Extrinsic impurity (such as N_2 and Ne) seeding has also been successfully employed to establish detachment in W7-X plasmas [36].

A notable observation in W7-X detached plasmas (DPs) is a robust up-down asymmetry in impurity radiation, despite the up-down symmetric magnetic topology in the observed triangular plasma cross-sections by the bolometer system [37]. This work focuses on plasmas, where intrinsic carbon (from the graphite targets) is the main impurity species. The bolometer tomography [38] has revealed dynamic 2D radiation patterns, especially a multi-X-point radiation (multi-XPR) structure that shows finer spatial features compared to the oxygen dominant radiation in OP1.2a [38].

Comparisons between radiation patterns in forward-field experiments (the normal toroidal magnetic field direction: counterclockwise from the top view of W7-X) and reversed-field experiments indicate that the major asymmetric feature reverses, suggesting a strong influence of $\mathbf{E} \times \mathbf{B}$ drift. These results have been consistently observed by visible video cameras [39, 40]. While 3D simulations with the EMC3-Eirene code [41, 42] have shown poloidal asymmetries in impurity radiation, the experimentally observed up-down asymmetry remains unexplained. This work shows for the first time the observed multi-XPR structure and its dynamics in the DP regime in W7-X and also the investigations on how the $E \times B$ drift, in particular its poloidal component,

influences the radiation symmetry in the DP phases. Future studies will compare these results with detachment scenarios caused by extrinsic impurities (see [34]). The up/down asymmetry in the radiation distributions in the attached plasma phase (see figure 6(*a*) in section 3.2) is more strongly influenced by impurity sources closely related to the flows of the background ions, which exhibit varying degrees of asymmetry due to $E \times B$ drift, as observed experimentally both in tokamaks [43–45] and stellarators [46–49]. These investigations are future tasks that require improved particle flux measurements (see section 2.2 and appendix B).

The paper is structured as following. Section 2 describes the experimental setup, plasma conditions, and key diagnostics. Section 3 presents general observations from a representative experimental program (XP). Section 4 examines field-reversal experiments. Section 5 compares experimental results with 3D modeling and uses a simplified model to discuss how poloidal $\mathbf{E} \times \mathbf{B}$ drift influences impurity transport and radiation asymmetry. Section 6 summarizes the work.

2. Experimental conditions and key diagnostics

2.1. Magnetic configuration and boundary conditions

The W7-X stellarator (major radius $R = 5.5$ m, minor radius $a \approx 0.5$ m) is equipped with ten carbon divertor units, symmetrically arranged in five modules (M1 to M5). Each module contains two divertor units—one upper (M11 to M51) and one lower (M10 to M50)—preserving the stellarator's flip symmetry. Each divertor unit consists of a horizontal and a vertical target with a pumping gap in between (see figure 1(*b*) and (*c*)), which is a designated area with cryo-pumps that allows for the removal of neutral particles and impurities from the plasma edge. The plasmas analyzed in this study correspond to the SDC, characterized by five topologically independent magnetic islands with a rotational transform of $\iota = n/m = 5/5$, where m and n are the poloidal and toroidal mode numbers, respectively. The magnetic topology is non-axisymmetric with five-field-period ($n = 5$), and the plasma cross-sections vary toroidally from triangular to bean-shaped. All this is shown in figures 1(*a*)–(*d*). The five resonance magnetic islands (in color bands) share the five X-points (labeled X1-X5 in figure 1(*d*)), where the island-divertor-relevant poloidal field component $B_p = 0$. The X-points toroidally follow the rotational transform at the LCFS, $\iota(r = a) = \mathrm{d}\theta/\mathrm{d}\phi = 1$, and shift poloidally by $\Delta\theta = 2\pi/5$ (i.e. 72°) per field period ($\Delta\phi = 72°$). These islands are intersected by different divertor targets (see figures 1(*a*)–(*c*)). The width of the formed SOL is ∼7 cm.

The triangular cross-sections do not contain any divertor elements, which can be seen in figure 1(*d*) with the example of the cross-section at $\phi = 108°$ that is monitored by the bolometers. The magnetic structure is up-down symmetric, as the overlaid Poincaré plot shows. The outermost regions are located in the shadow of the divertor target, where the field lines end on different sections of the divertor targets. Figure 2 uses selected flux tubes to illustrate the connections of the five magnetic islands in the triangular cross-section to the nearest divertor targets. In general, the two upper islands (is1 and is2) are most closely connected to the upper horizontal targets in M31 and M21 (labeled U_H_M3 and _M2), while the two lower islands is4 and is5 are closest to the lower horizontal targets in M30 and M20 (labeled D_H_M3 and _M2). The island on the inboard side (is3) is connected to the vertical targets in M21 and M30 (labeled U_V_M2 and D_V_M3). This figure provides valuable information about the shortest transport path of carbon impurities released from the target reaching the triangular cross section where the multi-XPR structure is observed.

The distribution of the magnetic connection length L_c (wall-to-wall) in the triangular cross-section is calculated using the EMC3-lite code [50] using vacuum magnetic topology, without considering the error field effects. These error fields [51], arising from the finite deformation and misalignment of the superconducting coils, can alter the edge magnetic topology of the plasmas under study, therefore corrections with trimming coils [52] has been applied, although they are unlikely to fully compensate for the error fields. Furthermore, we ignore the effect from plasma currents [53], as it is small in the studied plasmas. In figure 3(*a*), the L_c values are only shown for the upper region, while those for the lower region are not shown due to the up/down symmetry.

For completeness, the map about the L_c distribution at the divertor targets is shown in figure 3(*b*). It can be seen that due to the discrete nature of the divertor targets in W7-X, three distinct SOL regions can be identified: (1) island SOL—the region shares the LCFS with the confinement region ($L_c >$ 300–500 m), (2) private flux region (PFR)—the region between two neighboring islands ($L_c \sim 100$ m), and (3) target shadow region (TSR)—regions where L_c is shorter than the toroidal circumference of W7-X ($L_c < 2\pi R \sim 35$ m).

It is to be expected that the PWI regions on the targets are typically located within the island SOL with longer L_c values. However, particles and energy can enter the TSR (or PFR) via cross-field transport. This process is schematically illustrated in figure 3(*c*).

2.2. Diagnostics

The key diagnostics used in this study are briefly described below.

- ***Bolometer system.*** it consists of a horizontal bolometer camera (HBC, 32 channels) and a vertical bolometer camera (VBC, with two sub-cameras, 24 channels each) [37]. The detector is of the metal-resistance type [54] with a blackened gold absorber (5 μm thick) that has a broad spectral sensitivity covering the visible, VUV, and soft x-ray ranges. Their line-of-sight (LoS) arrangements are also shown in figure 1(*d*). The LoS of the HBC are up/down symmetric, and the channels with geometrically up/down symmetric LoS (e.g. ch5 and ch28 shown in figure 1(*d*)) can directly monitor radiation (a)symmetry. In combination with VBC measurements, 2D radiation distributions have been obtained based on tomography using the relative gradient

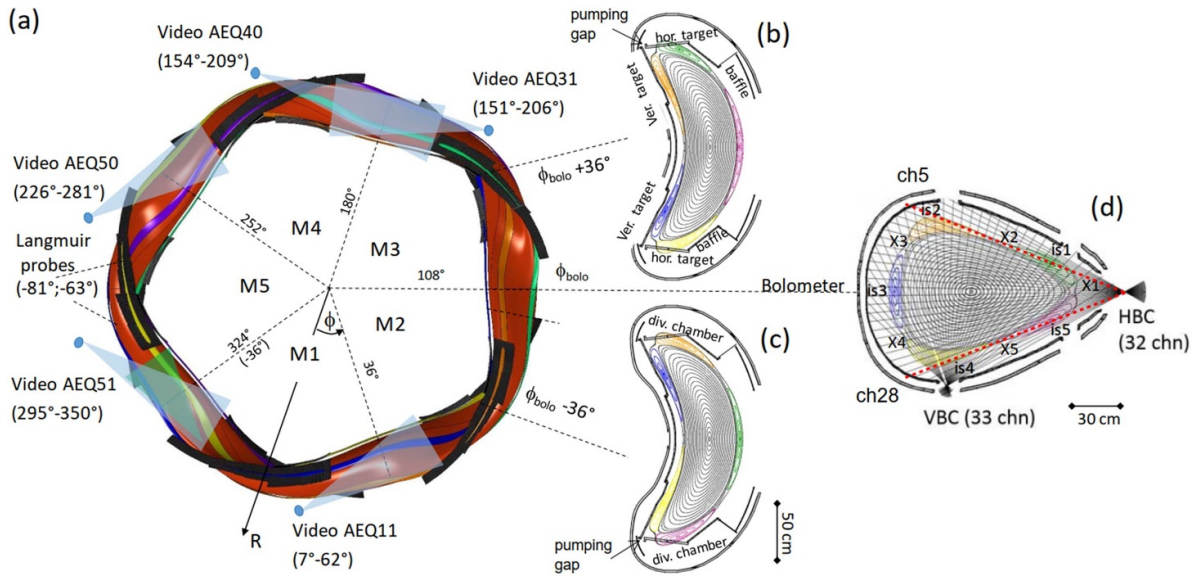

Figure 1. (*a*) Top view of W7-X with the five pairs of divertor units (black), each consisting of a horizontal and a vertical target with a pumping gap in between (see (*b*) and (*c*)), installed with stellarator symmetry in the five modules (labeled M1 to M5) and the selected key diagnostic positions. The five color bands represent the five magnetic resonance islands in the SDC. (*b*) and (*c*) Show Poincaré plots of two bean-shaped planes in M3 and M2, respectively, while (*d*) presents the triangular cross-section between them (at $\phi_{\rm bolo} = 108°$) as viewed by the bolometers, featuring an up/down symmetric magnetic topology. The LoS arrangement of the bolometers, HBC and VBC, is also depicted in (*d*). The five magnetic islands (is1 to is5) and the five X-points (X1 to X5) are labeled. The two red dashed lines in (*d*) indicate the LoS of ch5 and ch28 in the HBC, which directly provide up/down symmetry information on radiation in the SOL.

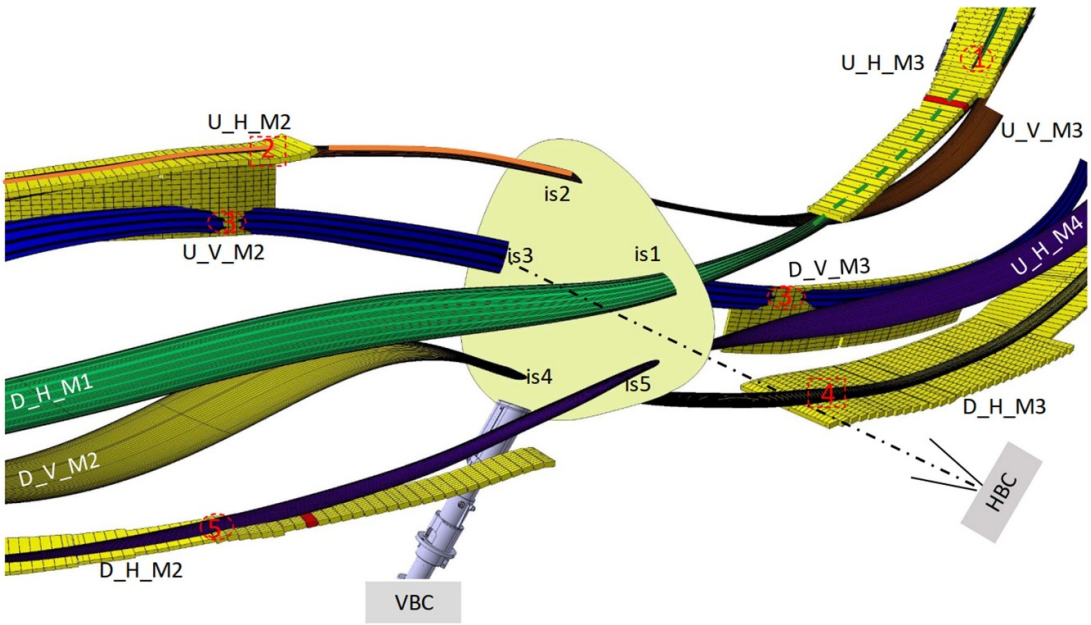

Figure 2. Illustration of five selected flux tubes in the five magnetic islands (is1 to is5) passing through the triangular cross-section monitored by the bolometers and intersecting the nearest target plates in M2 and M3. The intersections are labeled according to their corresponding island number.

smoothing (RGS) method [38]. To obtain the total radiated power loss $P_{\rm rad}$, the radiation from the HBC observation volume is extrapolated to the whole plasma volume [32]. Possible toroidal variations in radiation intensity are small for the higher radiation phases investigated, as confirmed by EMC3-EIRENE calculations at different toroidal positions, and are therefore not considered. Alternatively, it can be determined from the tomographic reconstruction ($P_{\rm rad\_2D}$), which offers a higher accuracy, especially when the plasma radiation exhibits strong poloidal asymmetry. The uncertainty in $P_{\rm rad}$ based on the HBC measurements is ∼10%–15%, as the poloidal asymmetry is not taken into account.

- ***Visible video cameras.*** the system provides an overview of the plasma, the vacuum vessel and the PFCs in W7-X

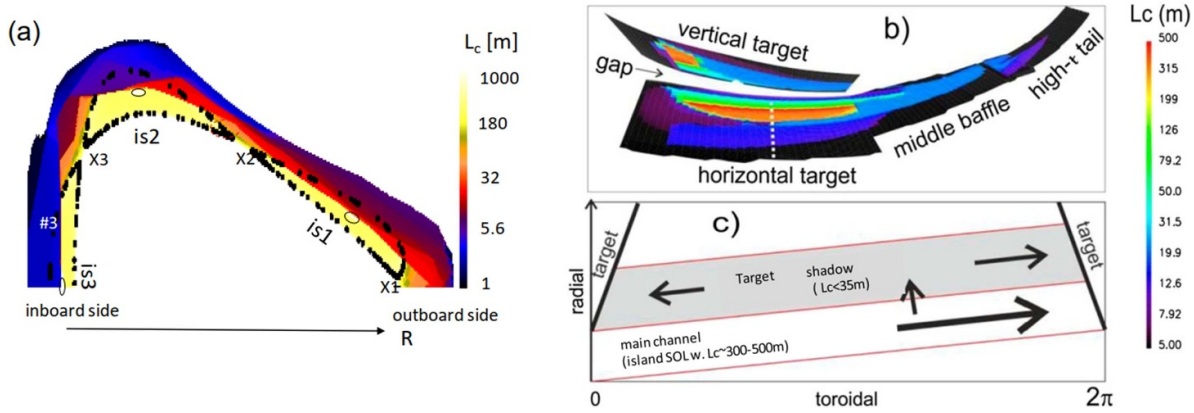

Figure 3. The wall-to-wall connection length L_c in the upper SOL in the triangular cross-section (*a*) and that at the divertor targets (*b*). (*c*) A schematic representation of parallel and perpendicular transport in the main transport channel (i.e. island SOL) in contact with the SOL–core interface and with the target shadow. The dashed white line in (*b*) indicates the location of a LP array on the horizontal target. Note the different color bars in (*a*) and (*b*). (*b*), (*c*) Reproduced from [10]. © EURATOM 2021. CC BY 3.0.

[39, 40]. A total of ten cameras are installed in tangential ports (AEQ), two cameras per module. They detect line emission in the 520–720 nm range and provide a 3D perspective of the edge plasma radiation, e.g. from CII, CIII and Hα. The FoV of each camera has a toroidal extent of $\sim$55°, covering the triangular cross-section of the respective module. These images are compared with the 2D radiation profiles from bolometer tomography. The spatial resolution is approximately 1–2 mm. The locations of the cameras used in this study are indicated in figure 1(*a*).

- ***Infrared (IR)-cameras.*** Five pairs of IR-cameras are installed equidistantly in the five modules, each with stellarator symmetry. They measure the temperature distributions over the individual target surfaces and can provide the heat load profiles and the integrated value of the heat load, P_{div}, over the target elements, including the horizontal and vertical plates [55, 56]. Information on the up/down asymmetry of the target heat load can be obtained (see figure 5), but this poses a challenge for the study of drift effects in the SDC plasmas investigated, as the error fields are not fully corrected [51, 57].
- ***Divertor visible light cameras.*** A set of visible cameras is equipped with a narrow-band filter to record the representative optical transitions of the most interesting species (such as H and C) in the W7-X plasmas [58]. They are mounted in immersion tubes, shared with IR-cameras. The measurements relevant to this work are the Balmer alpha line of the hydrogen atom (656.28 nm; H_α) and the CII emission (514.3 nm) in front of the target modules. The intensity of the H_α and CII line emission contains information about the recycling flux and the impurity level near the targets, respectively.
- ***Langmuir probes (LPs).*** The particle fluxes on the targets are monitored by the LPs on the basis of the mean ion saturation current J_s. The probes consist of two arrays of ten probes each, which are embedded in the upper and lower horizontal target (in M5; see figures 1(*a*) and 3(*b*)) in stellarator symmetry at $\phi = -63°$ and $\phi = -81°$, respectively [59]. For the SDC, the probes do not cover the entire plasma-target interaction zone (see also figure 17), which limits the diagnostic capability [57]. The target temperature $T_{\mathrm{e,t}}$ and the density $n_{\mathrm{e,t}}$ (see figures 4 and 19) are evaluated within the framework of Bayesian modeling [59].
- ***Neutral gas pressure gauges.*** The neutral gas pressure gauges at W7-X are ionization pressure gauges with LaB_6 emitters. For the relevant experimental campaign, 13 gauges are installed at various locations [60], including in the midplane of the plasma vessel and at the pump ports connected to the divertor chambers. Among them, a pair of gauges are located in the upper and lower divertor chambers (see figures 1(*b*) and (*c*)) in ports AEH31 and AEH30 (in M3), which are installed stellarator-symmetrically and can provide information on asymmetries on neutral gas pressure. A detailed description and an overview of the experimental results at W7-X can be found in [60–62], respectively.

Other parameters such as the main plasma density and temperature around the LCFS, the line-averaged density $<n_e>$, and the diamagnetic energy W_p are measured by Thomson scattering [63, 64], a dispersion interferometer [65] and a diamagnetic loop [66], respectively. The effective ion charge Z_{eff} is from the visible bremsstrahlung measurements [67].

3. Experimental results

3.1. General observations in transitions from attached to DP

Plasma detachment in W7-X is primarily governed by the power balance between the power P_{rad} radiated by impurities, the power P_{div} incident on divertor targets and the power for ionization of recycling neutrals P_{ion} [10]. In a quasi-steady state, they satisfy the global power balance $P_{\mathrm{heat}} = P_{\mathrm{rad}} + P_{\mathrm{div}} + P_{\mathrm{ion}}$, where P_{heat} is the effective heating power. Assuming complete recycling (recycling neutral flux Γ_0 = particle flux $\Gamma_i \equiv \Gamma_t$), the total particle flux relates to the

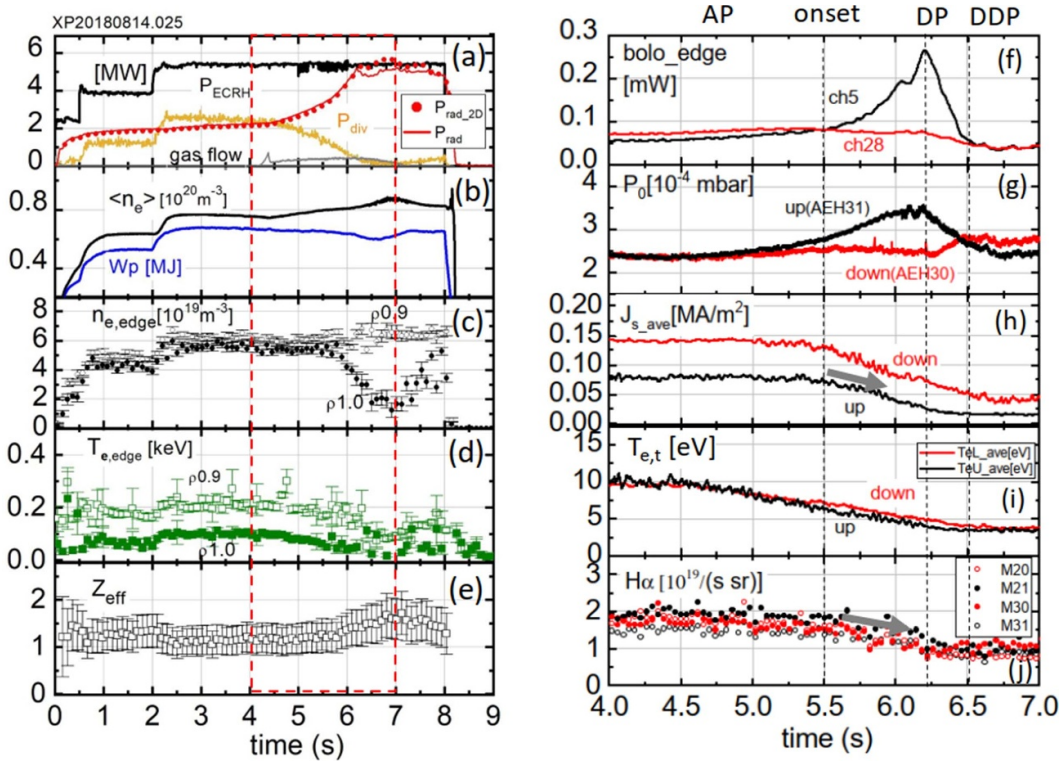

Figure 4. (*a*)–(*e*) Time traces of key plasma parameters in XP25. (*f*)–(*j*) Measurements of edge diagnostics in the investigated plasma phases ($t = 4.0$–7.0 s), marked by the rectangle in (*a*)–(*e*), where three dashed lines correspond to the onset of the DP phase ($t = 5.5$ s), the DP with the strongest up/down asymmetry ($t = 6.2$ s) and the deep DP phase ($t = 6.5$ s).

radiation loss fraction ($f_{\rm rad} = P_{\rm rad}/P_{\rm heat}$) as follows

$$\Gamma_t = kP_{\rm heat}\,(1 - f_{\rm rad})\,, \tag{1}$$

where $k = (\gamma_{\rm t}T_{\rm t} + E_{\rm i})^{-1}$, and $(\gamma_{\rm t}T_{\rm t})$ represents the energy transferred by an electron–ion pair at an averaged ion and electron temperature $T_{\rm t}$. The total sheath energy transmission factor is approximately $\gamma_{\rm t} \approx 7$, and $E_{\rm i}$ denotes the total energy cost per ionization event. This relation implies that once $T_{\rm t}$ drops below $E_{\rm i}$ /$\gamma_{\rm t}$, further increasing $f_{\rm rad}$ reduces both the ion flux and the associated $P_{\rm div}$. This behavior is demonstrated below by an experimental density ramp program. It is important to note that volume recombination and charge-exchange (CX) processes are not considered here, as EMC3-Eirene simulations indicate that their contributions are small in the studied plasmas [10, 68].

The representative discharge analyzed in this study is XP20180814.025 (hereafter XP25). Key plasma parameters are shown in figures 4(*a*)–(*e*). The investigated plasma phase corresponds to the period from $t = 4.0$ s to 7.0 s heated by the 5.5 MW ECRH during gas refueling (shown in gray in panel (*a*), arbitrary units). This time interval is marked by a rectangle, and the evolution of the boundary plasma parameters during this period is shown in figures 4(*f*)–(*j*).

For $t > 4.0$ s, the plasma density $<n_{\rm e}>$ increases due to gas refueling, which leads to a steady increase in radiated power until the radiation fraction $f_{\rm rad}$ approaches unity. Up to $t = 6.2$ s, both $P_{\rm rad}$ from HBC measurements and $P_{\rm rad\_2D}$ from bolometer tomography show consistency. At the same time, the total heat load of the divertor $P_{\rm div}$ (i.e. the sum of the heat load of all divertor targets) decreases by more than one order of magnitude. With a further increase of $<n_{\rm e}>$, $P_{\rm div}$ remains at its low level (corresponding to the detection limits of the IR cameras), while a discrepancy of ∼10% between $P_{\rm rad}$ and $P_{\rm rad\_2D}$ becomes visible (see figure 4(*a*)). The decrease of $P_{\rm rad}$ is related to the variation of the radiation patterns, which typically indicates a phase change of the poloidal asymmetry in the 2D radiation profile (see later figures 6(*e*) and (*f*)).

During this time interval, the plasma undergoes transitions from the attached plasma (AP) phase to the DP phase and finally to the deep DP phase. The onset of the DP phase is defined by a decrease in the particle flux, which is represented by measurements of the ion saturation current. Figure 4(*h*) shows the average ion saturation current $J_{\rm s\_ave}$ obtained from LP measurements at the upper (black) and lower (red) divertor target, and a vertical dashed line at $t = 5.5$ s ($f_{\rm rad} = 0.6$ and $<n_{\rm e}> \ 0.8 \times 10^{20}$ m^{-3}) marks the onset of the DP phase. During the DP phase, as $f_{\rm rad}$ increases, the edge temperature $T_{\rm e,edge}$ at $\rho = 1.0$ decreases from ∼100 eV to ∼20 eV, while the edge density $n_{\rm e,edge}$ (at $\rho = 1.0$) declines from $\sim 5 \times 10^{19}$ m^{-3} to $\sim 2 \times 10^{19}$ m^{-3}. The value of $T_{\rm e,edge}$ at $\rho = 0.9$ shows a similar trend to that at $\rho = 1.0$, but with clearly higher values, while the value of $n_{\rm e,edge}$ at $\rho = 0.9$ remains almost unchanged. This, together with the considerable drop in the value at $\rho = 1.0$, indicates a steepening of the density profile in the outer confinement region, which normally

influences particle and energy transport at W7-X [69]. These values are determined by Gaussian process fits [70] applied to the Thomson scattering data, since the raw data in the edge plasma region are usually highly uncertain. The transition from the DP phase to the deep DP phase ($t > 6.2$ s) is indicated by a slight decrease in the plasma stored energy W_P (by a factor of ∼10%). In addition, the $Z_{\rm eff}$ value increases from ∼1.2 to ∼1.5, indicating an increased penetration of impurities through the LCFS, and the radiation fraction within the LCFS increases (from ∼15% in the AP phase) to ∼60% (see figure 9(*b*)), which is accompanied by a significant change in the radiation pattern (see figures 6(*e*) and (*f*)).

The diagnostic monitors the up/down asymmetry of the boundary plasma parameters, making the following key observations:

i. The **edge radiation asymmetry** directly detected by the HBC channels (ch5 and ch28) is shown in figure 4(*f*). After the onset of the DP phase ($t > 5.5$ s, up to $t = 6.2$ s), ch5, which measures weaker radiation in the upper SOL during the AP phase, gradually surpasses ch28, suggesting enhanced radiation from the upper SOL. This up/down asymmetry reaches its maximum at $t = 6.2$ s and decreases during the transition from the DP to the deep DP phase ($t > 6.2$ s), almost disappearing at $t = 6.5$ s. The evolution of radiation distributions obtained by bolometer tomography is displayed in figure 6.

ii. The **neutral hydrogen pressure** (P_0) measured in the upper and lower divertor chambers (H31 and H30) shows a similar asymmetry trend as the edge radiation (see figure 4(*g*)). After the onset of detachment, P_0 in the upper chamber consistently exceeds the value in the lower chamber, and the up/down asymmetry also reaches its maximum at $t = 6.2$ s. During the transition from DP to deep DP, this asymmetry decreases. These relationships reflect the cooling effect of the impurity radiation on the SOL temperature, with higher radiation leading to a lower SOL temperature and a longer penetration length of the neutral particles (λ_0), which increases the neutral hydrogen pressure. Note that in the deep DP phase, the λ_0 value is ∼several cm, which is ∼10 times longer than in the AP phase [10].

iii. The **averaged target temperatures** $T_{\rm e,t}$ of the upper LPs and the lower LPs are shown in figure 4(*i*). They are close to each other and drop from ∼10 eV in the AP phase to ∼3.5 eV in the deep DP phase. Of all the probes, the upper LP10 records the highest temperature in the AP phase (∼18 eV) (see figure 19(*a*)). During the DP phase, the average ion saturation currents of both the upper and lower target probes decrease with increasing $f_{\rm rad}$, with significantly higher values for the lower targets (figure 4(*h*)). This seems to indicate the up/down asymmetry in particle flux that was observed in W7-AS [46] and LHD [48] and was also investigated in the 'low-iota' magnetic configuration in W7-X [47, 49]. However, direct quantification of the asymmetry of the total particle flux is not possible due to the incomplete coverage of the LPs over the strike zones for the plasmas studied in the SDC configuration (see also appendix B).

iv. The **H_α measurements** near the upper (M21, M31) and lower (M20, M30) targets in modules M2 and M3 are shown in figure 4(*j*). The signals generally follow each other. Overall, H_α emission intensity decreases by ∼50% in the deep DP phase compared to the AP phase, indicating a significant reduction in recycling flux. This trend is consistent with 3D modeling results, which suggest that neutral recycling weakens due to a reduced power fraction available for neutral particle ionization [10].

In addition, figures 5(*a*), (*b*) and (*c*), (*d*) show the **heat load distributions** on the upper and lower divertor targets at the onset of the DP phase ($t = 5.5$ s, $f_{\rm rad} \sim 0.6$) and in the deep DP phase ($t = 6.5$ s, $f_{\rm rad} \sim 1.0$). These heat load distributions are obtained by averaging the data of all available upper target plates (M11 to M51) and lower target plates (M10 to M50) to minimize the error field effects. The strike zones, where high-energetic particles are deposited, are clearly shown in figures 5(*a*) and (*b*) on both the horizontal and vertical targets plates. Those in the TSR (e.g. at $\phi \sim -18^\circ$ on the horizontal targets; cf. $L_{\rm c}$ values in figure 3(*b*)) are the result of the cross-field transport of particles. Discrepancies between the patterns in figures 5(*a*) and (*b*) are still visible: (1) the strike zone on the lower horizontal target plate is further from the pumping gap than that on the upper target plate, (2) the lower horizontal target plate experiences a visibly higher peak heat flux (∼2.0 MW m^{-2}) than the upper target plate (∼1.7 MW m^{-2}). This up/down asymmetry contains valuable information about drift effects, based on which the $\mathbf{E} \times \mathbf{B}$ drift in the W7-X plasmas in the 'low-iota' magnetic configuration is studied [47], where the edge topology is not so sensitive to the error fields as in the SDC.

A further analysis shows that the degree of asymmetry of the peak value and the profile width of the heat flux decreases with increasing $f_{\rm rad}$. Up to $f_{\rm rad} > 0.9$, an almost homogeneous heat removal occurs from both the upper and lower target plates, accompanied by the significant reduction in the peak heat flux, as shown in figures 5(*c*) and (*d*). Detailed information on the temporal development of the heat load profiles at representative toroidal positions is shown in figures 17(*a*) and (*b*) in appendix B to provide a complete picture.

3.2. Observation of the multi-XPR with up/down asymmetry: bolometer results

2D radiation profiles. The bolometer tomography has been performed for XP25. The 2D radiation profiles obtained for the triangular plasma cross-section at selected time points are presented, with the result for the AP phase at $t = 3.0$ s ($f_{\rm rad} = 0.4$) also included for completeness. Figures 6(*a*)–(*d*) shows the 2D profile evolution from the AP to the DP phase ($f_{\rm rad} = 0.6$–0.9), while figures 6(*e*) and (*f*) illustrates the transition from the DP to the deep DP phase ($f_{\rm rad} > 0.9$). The chord brightness profiles for the HBC and the VBC, which serve as inputs for the bolometer tomography, are available in figure 16

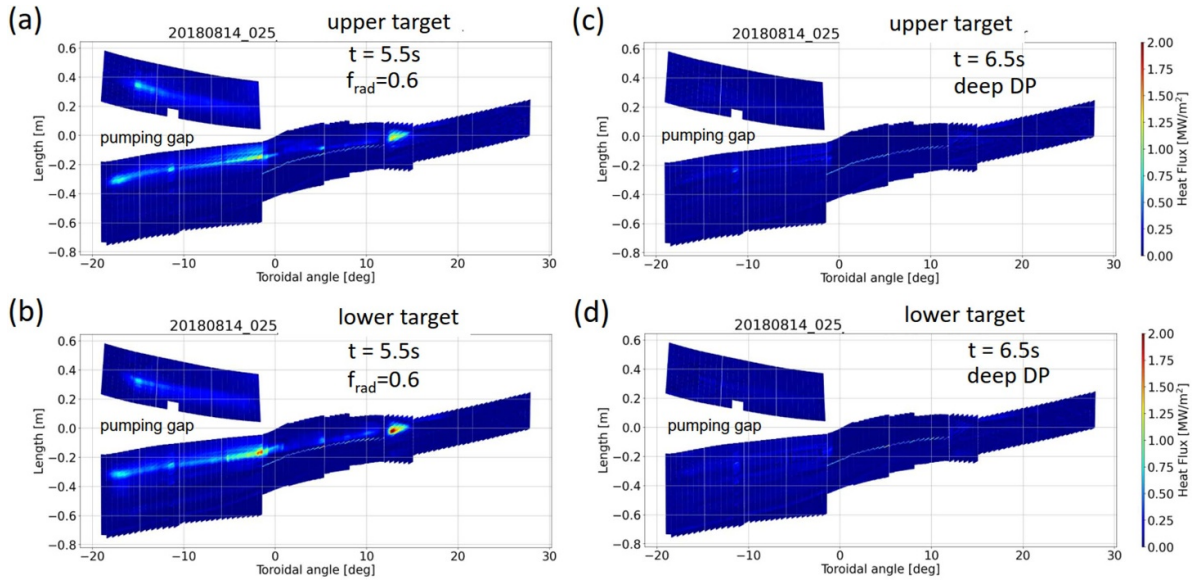

Figure 5. The averaged heat loads of the upper and lower divertor targets in XP25 at the onset of the DP phase ($t = 5.5$ s, $f_{\rm rad} \sim 0.6$) ((*a*) and (*b*)) and in the deep DP phase ($t = 6.5$ s, $f_{\rm rad} \sim 1.0$) ((*c*) and (*d*)), the former showing the up/down asymmetry and the latter showing the almost complete dissipation of the incoming power flux on the targets by impurity radiation.

in appendix A. In general, these 2D radiation profiles show all edge-localized radiation zones that are unevenly distributed in the poloidal direction. The comparison of the emissivity in the upper and lower SOL shows a clear up/down asymmetry. The dynamics with increasing $f_{\rm rad}$ are as follows:

- **AP phase ($f_{\rm rad} = 0.4$; $<n_{\rm e} > 0.75 \times 10^{20}$ m^{-3}).** The emission zones are located radially near the TSR (see figure 3(*a*)), with the lower islands (is5 and is4) radiating considerably stronger than the upper islands (is1 and is2). The emission in is5 is mainly located around the O-point and has a clear poloidal extension. Interestingly, there is a pronounced 'hot spot' in is3 in the upper interior region. These localized radiation zones are typically observed in the normal magnetic field direction and are thought to be associated with drift effects (see discussions in section 5.2).
- **DP phase ($f_{\rm rad} = 0.6$–0.9; $<n_{\rm e}> \sim 0.8 \times 10^{20}$ m^{-3}).** As the detachment progresses with increasing $f_{\rm rad}$, the primary radiation zones, such as in is3 and is4, shift radially inwards and poloidally toward the nearest X-point, which is already recognizable at detachment onset (figure 6(*b*)). In addition, the radiation around the upper X-point (X2) gradually intensified and becomes much more intense at $t = 6.2$ s, while the radiation near the lower X5 remains weaker. A multi-XPR structure with an up/down asymmetry is formed. This asymmetry exhibits a much brighter XPR around the upper X2 (peak emissivity $\sim$2.4 W cm^{-3}) than that around the lower X5 (by a factor of $\sim$4) and almost twice that of the other two X-points (X3 and X4) (see figure 6(*d*)). This feature of the multi-XPR structure is robust during the progressive plasma detachment in W7-X, which is caused by the radiation of intrinsic carbon impurities (see also the video images). The mechanisms responsible for this are discussed in section 5.2.
- **Transition to deep DP phase ($f_{\rm rad} > 0.9$–1.0; $<n_{\rm e}> \sim 0.9 \times 10^{20}$ m^{-3}).** At $t > 6.2$ s, the plasma transitions from the DP to the deep DP phase following a slight increase in the plasma density $<n_{\rm e}>$, which is marked by a significant variation in the 2D radiation patterns (see figures 6(*e*) and (*f*)): the brightness around the X2 weakens while that around the two inboard X-points (X3 and X4) increases. The localization of intense radiation zones at the inboard side is consistent with EMC3-Eirene simulations (see figure 14(*c*)), which suggest that the elevated neutral particle density plays a key role. In this phase, both hydrogen and impurity neutrals have an increased penetration length ($\sim$several cm, comparable to the island width) [10]. This newly developed multi-XPR structure exhibit only a slight up/down asymmetry, which is probably associated with neutral particle sources.

Further analyses have been performed on the details of the radiation dynamics with increasing $f_{\rm rad}$. The results are presented below.

The up/down asymmetry degree in the radiation zones of the island SOL is calculated. Each studied magnetic island is divided into three equal poloidal sections, as shown in figure 7(*a*) using the upper is2 as an example. Each section spans poloidally $\Delta\theta_{\rm is}/3$, where $\Delta\theta_{\rm is} = 72^\circ$ corresponds to the poloidal extent of the island. The right and left sections (labeled is2_R and is2_L) are considered to be the region of X2 and X3, respectively. The radiated power in these sections are calculated as $P_{\rm rad,X} = 2\pi R \Sigma \varepsilon_i A_i$, where ε_i represents the

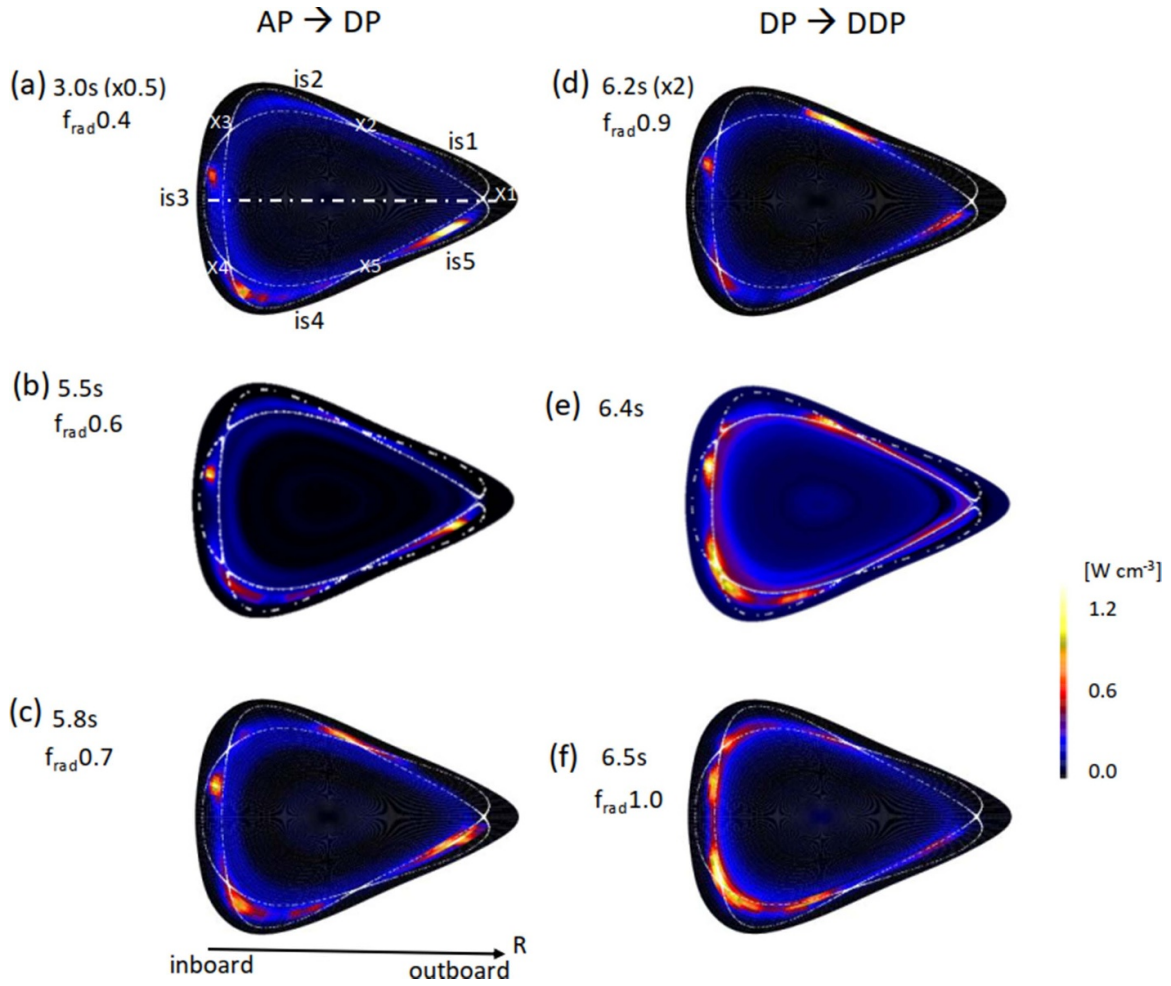

Figure 6. 2D radiation profiles from bolometer tomography at selected time points in XP25: (*a*)–(*d*) evolution from the AP to the DP phase, where panel (*d*) shows the strongest up/down asymmetry between the upper X2 and lower X5; (*e*), (*f*) transition from the DP to the deep DP phase, characterized by a shift in poloidal asymmetry. The X-points (X1–X5) and islands (is1–is5) are labeled in (*a*) for reference, which a horizontal dashed line at $Z = 0$ dividing the cross section equally into upper and lower regions. White lines indicate the separatrix. Color bars for (*b*), (*c*) and (*e*), (*f*) are shown to the right; in (*a*) the values are scaled by 0.5, while in (*d*) they are scaled by a factor of two.

emissivity in the *i*th grid element with an area A_i in the bolometer tomography. The ratio of the radiated power in the upper and lower X-point regions with identical magnetic structure, $f_{\mathrm{asy},X} = P^{\mathrm{up}}_{\mathrm{rad},X}/P^{\mathrm{down}}_{\mathrm{rad},X}$, is then determined, which represents the asymmetry degree.

The most interesting results of $f_{\mathrm{asy},X}$ are shown in figure 7(*b*) as a function of f_{rad}: (1) the value of $f_{\mathrm{asy},X}$ based on the $P_{\mathrm{rad,X}}$ in the right sections of is2 and is4, which mainly represent the up/down asymmetry in the radiation around the upper X2 and lower X5 (in red circles; labeled 'is2_R vs is4_R'). It has a value of $f_{\mathrm{asy},X} \sim 1$ for phases with lower f_{rad} (0.4–0.6) before the onset of DP, increases almost linearly with f_{rad} during the DP phase ($f_{\mathrm{rad}} = 0.6$–0.9) reaching a maximum of $\sim$4, and drops to $f_{\mathrm{asy},X} \sim 1$ in the deep DP phase ($f_{\mathrm{rad}} \sim 1$; the up/down asymmetry almost disappears). (2) The $f_{\mathrm{asy},X}$ about the $P_{\mathrm{rad,X}}$ in the left sections of is2 and is4, which already exhibits a strong asymmetry in the AP phase, has a typical value of $f_{\mathrm{ratio}} \sim 0.4$ (in black circles; labeled 'is2_L vs is4_L'), which remains nearly constant across different radiation fractions. (3) The asymmetry in is3, which appears as an 'outlier' whose peak emissivity is higher in the upper region than in the lower region (blue circles; labeled 'is3_U vs is3_L'), has a $f_{\mathrm{asy},X}$ value varying between 0.9 and 1.1.

The radiation zones in is5 and its counterpart is1 are not analyzed as they are mainly located around the O-points.

Radiation zone movement and X-point radiation condensation are further analyzed by examining the radial positions of the peak emissivity in selected magnetic islands (e.g. is2, is3, and is4) and the radially averaged emissivity in the edge region ($\Delta r_{\mathrm{eff}} = 1.5$ cm and $\rho > 0.9$).

Figure 8 (left) shows the radial position of the peak emissivity as a function of f_{rad}, which shifts radially inward with increasing f_{rad} from $\rho = r_{\mathrm{eff}}/a = 1.1$ to $\sim$1.0 (corresponding to $\Delta r_{\mathrm{eff}} \sim 5$ cm). Here, the minor radii r_{eff} outside the LCFS in the SOL are estimated using the grids in the bolometer tomography via linear extrapolation of the magnetic structure near the LCFS [38]. This shift of the radiation layer toward the LCFS can alternatively be displayed by radial 1D radiation profiles obtained by poloidal averaging of the

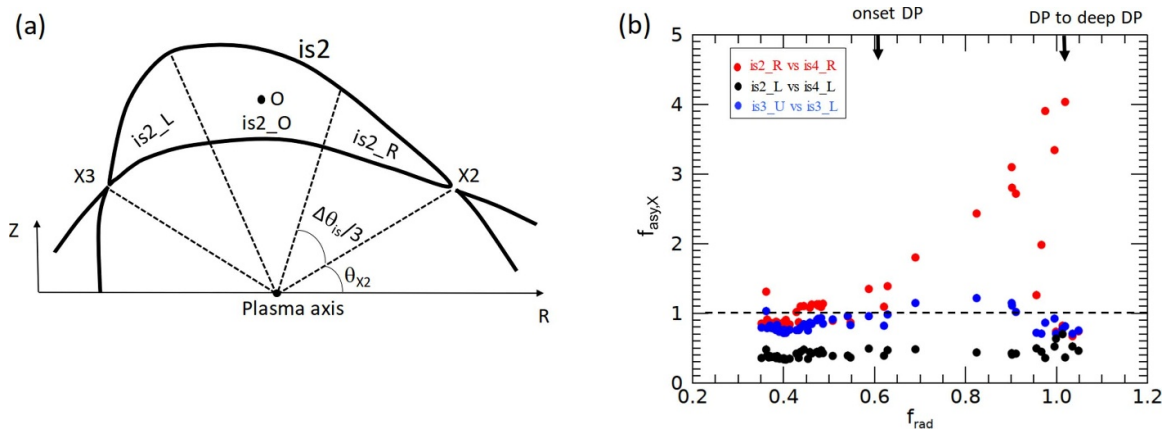

Figure 7. (*a*) Definition of X-point regions (for X2 and X3) using the upper island is2 as representative by dividing it into three equal poloidal sections (labeled is2_R, is2_O, and is2_L), where is2_R is designated as X2 region and is2_L as the X3 region. (*b*) The ratio of radiated power between the upper and lower X-regions in islands with identical magnetic topology $f_{asy,X}$ as a function of f_{rad} in XP25: upper X2 inside is2 vs. lower X5 inside is4 (in red circles; labeled 'is2_R vs is4_R'), upper X3 inside is2 vs. lower X4 inside is4 (in black circles; labeled 'is2_L vs is4_L'), and upper section vs. lower section in is3 (in blue circles; labeled 'is3_U vs is3_L').

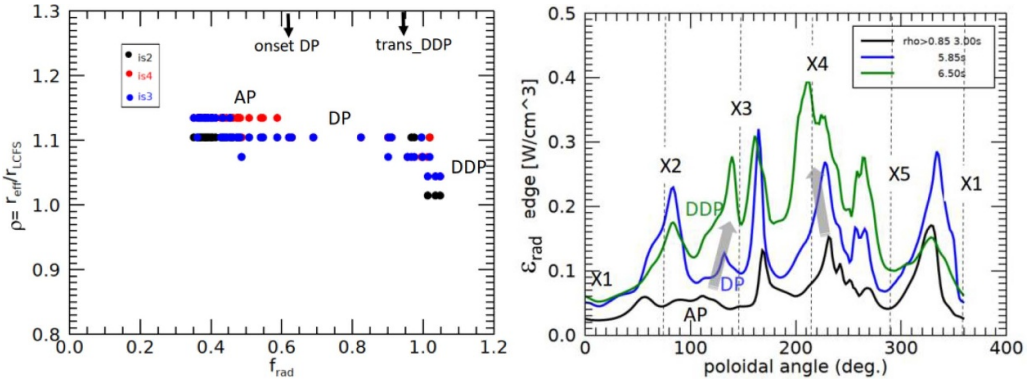

Figure 8. (Left) Radial shift of the emissivity peak within the magnetic islands (is2, is3, and is4) towards the LCFS with increasing f_{rad}. (Right) The radially averaged emissivity in the edge region ($\rho > 0.85$) as a function of the poloidal angle θ for three plasma phases: AP ($t = 3.0$ s), DP ($t = 5.85$ s), and deep DP (labeled DDP, $t = 6.5$ s) to represent the poloidal shift of the radiation zones towards the X-points with increasing f_{rad}. The vertical dashed lines mark the poloidal positions of the five X-points (X1–X5), with $\theta = 0^\circ$ defined by the X-point at the tip of the triangular cross-section (X1).

2D radiation distributions [42, 43]. The fact that the emission zones shift radially inwards with increasing f_{rad} is also observed in spectroscopic measurements at W7-X [71] and in 3D simulations with EMC3-Eirene code (see section 5.1). This shift correlates with the T_e reduction both at the targets and at the LCFS. During the AP phase, the T_e value in the SOL ranges from ~10 eV to ~100 eV, while in the DP phase from ~3 eV to ~20 eV (see figures 4(*d*) and (*i*)).

Figure 8 (right) shows the radially averaged emissivity as a function of the poloidal angle θ for three plasma phases: AP ($t = 3.0$ s), DP ($t = 5.85$ s), and deep DP (labeled DDP, $t = 6.5$ s). It shows in another way that the impurity radiation is increasingly concentrated around X2, X3 and X4 in the DP phase and around X3 and X4 in the deep DP phase. This again illustrates the dynamics of the multi-XPR structure and shows how the impurity radiation redistributes with increasing f_{rad}. 3D simulations using EMC3-Eirene code consistently show condensation of the X-point radiation (except for the up/down asymmetry) (see section 5.1) and suggest that the flux-surface expansion near the X-points is the main reason for this [72]. It is noteworthy that this concentration of carbon radiation at the X-points during detachment was also observed in the W7-AS stellarator [23].

Radiated power fractions within the LCFS and in the SOL are also determined. As the radiation zone moves radially inwards with increasing f_{rad}, the radiated power around and within the LCFS increases, while the power in the outmost region of the SOL decreases (due to temperature reduction). Figure 9(*a*) demonstrates the decreasing signal level of the two VBC channels monitoring the island SOL (ch22 and ch23, labeled SOL_ch) and the simultaneous increase in the signal aligned with the LCFS (ch21, labeled LCFS_ch) as a function of plasma density $<n_e>$. The brightness reduction in the island SOL occurs at $<n_e> \sim 0.8 \times 10^{20}$ m^{-3}, close to the threshold of detachment onset determined by the ion saturation current in figure 4(*h*).

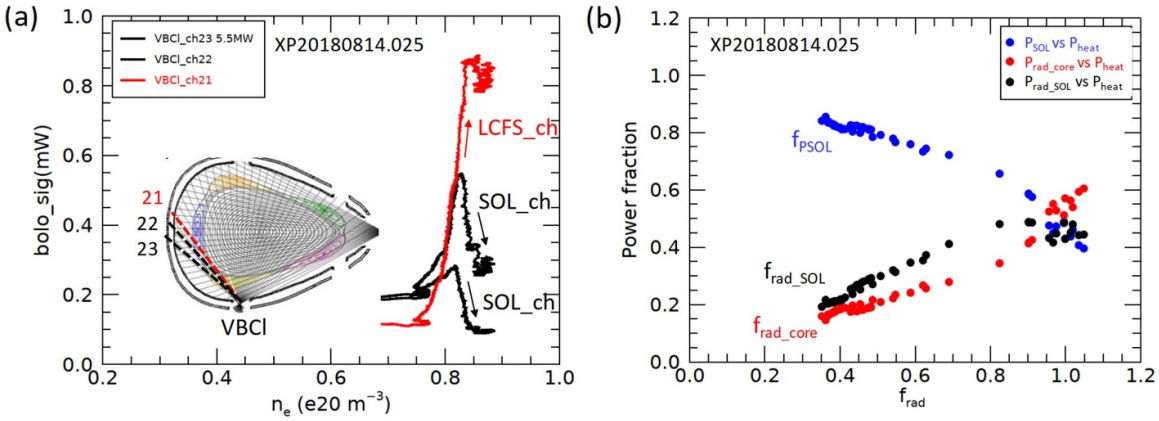

Figure 9. (*a*) The decreasing signal levels of the bolometer channels viewing the magnetic island (ch22 and ch23 in the VBCl, i.e. left part of the VBC) and the simultaneous increase of the signal of ch21 viewing the LCFS as a function of the plasma density $<n_e>$. The LoS of these channels are shown in inset. (*b*) The normalized power components, the power entering the SOL and the radiated power within the LCFS and in the SOL, as a function of f_{rad}.

The total radiated power $P_{rad,2D}$ based on the bolometer tomography is divided into the core radiation $P_{rad,core}$ (for $r_{eff}/a < 1$) and the SOL radiation $P_{rad,SOL}$ (for $r_{eff}/a \geqslant 1$). The corresponding core and SOL radiation fractions, defined as $f_{rad\_core} = P_{rad,core}/P_{heat}$ and $f_{rad\_SOL} = P_{rad,SOL}/P_{heat,}$ are shown in figure 9(*b*) as a function of f_{rad}. The level of f_{rad_core} increases from ∼15% in the AP phase to ∼60% in the deep DP phase, while the level of f_{rad_SOL} increases from ∼20% in the AP phase to ∼40% in the deep DP phase. The power fraction entering the SOL, defined as $f_{PSOL} = P_{SOL}/P_{heat}$ with $P_{SOL} = P_{heat}$-$P_{rad,core}$ is also shown there (in blue circles). It decreases from ∼85% in the AP phase ($f_{rad} = 0.35$) to ∼40% in the deep DP phase ($f_{rad} \sim 1.0$), with the latter corresponding to the SOL radiated power fraction $f_{rad\_SOL,}$ indicating a complete dissipation of the P_{SOL}.

3.3. Confirmation of the multi-XPR structure: video camera results

The images from the video cameras are analyzed to verify the multi-XPR structure obtained by the bolometer tomography and to gain insight into its 3D features. A correlation between the video diagnostics and the bolometer system is expected when carbon radiation is dominant at the low-T_e plasma edge. Since the camera monitoring the same module as the bolometers was not available for XP25, we have analyzed all other available cameras instead. For direct comparisons with the bolometer results, the spatially calibrated FoV of the cameras are overlaid with Poincaré plots for the SDC, including the triangular cross-sections, which have an identical magnetic structure to that viewed by the bolometers.

Figures 10(*a*)–(*c*) shows the temporal evolution of images from the camera AEQ50 ($\phi = 226°$ to $281°$) as a representative example with the following results. (1) In the AP phase ($t = 3.0$ s; serves as a reference), the bright emission zones correspond to the upper divertor region, the reflections of the wall elements and the impurity radiation bands passing through magnetic islands (e.g. is3 and is5). (2) In the DP phase ($t = 6.2$ s), a strong radiation belt helically aligned with the upper X-line (connecting the X-points in the three Poincaré plots), which is not seen in the AP phase. Other two intensive radiation bands pass through regions near X3 and X4, and the emissions from the divertor region and the reflections of the wall elements become weaker. In the triangular cross-section (red Poincaré plots), the up/down asymmetry in the upper and lower XPR (X2 and X5) is clearly seen, and the emission around the lower X5 is too weak to be detectable. The whole cross-section exhibits a radiation pattern closely resemble the bolometer results (see inset in figure 10(*b*)). (3) In the deep DP phase ($t = 6.5$ s), a clear attenuation of the radiation along the upper X-line (through X2), while the radiation bands around X3 and X4 on the inboard side become more pronounced (thicker and more intense). The radiation structure in the triangular cross-section is very similar to the bolometer results shown in figure 6(*f*).

Figure 11 shows images at the same time as figure 10(*b*) ($t = 6.2$ s, XP25) from cameras located at different toroidal positions (in different modules). The images from cameras AEQ11 ($\phi = 7°$–$62°$), AEQ31 ($\phi = 151°$–$206°$) and AEQ51 ($\phi = 295°$–$350°$) are representative and are shown in panels (*a*)–(*c*). It can be seen that these cameras capture images that are almost identical to those of AEQ50 in figure 10(*b*) (horizontally flipped), such as an intensive radiation band along the upper X-line (passing through X2) and the two intense radiation bands passing through X3 and X4 at the inboard side. Those in the triangular cross-section (red Poincaré plots) reconfirm the multi-XPR structure with the same up/down asymmetry of radiation between X2 and X5 observed by bolometer tomography, which appears consistently in other triangular plasma cross-sections in different toroidal modules.

Overall, the video diagnostics show that the multi-XPR structure extends toroidally as helical radiation bands across each module, preserving the field periodicity of W7-X. This also points to the fact that the effects of the not fully compensated error fields do not affect the field periodicity of the XPR. The initial hypothesis—that the radiation might

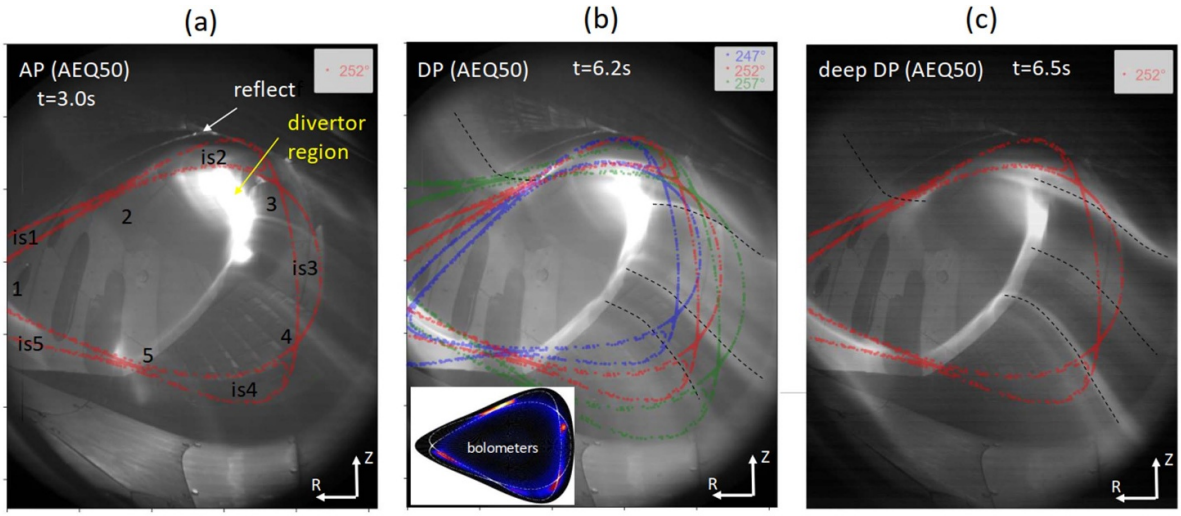

Figure 10. Time evolution of the images from the video camera AEQ50 in the AP (*a*), DP (*b*), and deep DP (*c*) phases in XP25. The five magnetic islands and X-points are labeled consistently in (*a*) with figure 6 for direct comparison with the bolometer results. Poincaré plots for the SDC at selected cross-sections ($\phi = 247^\circ$, 252° and 257°) are overlaid in (b) in blue, red and green, respectively, while only the triangular cross-section ($\phi = 252^\circ$) is shown in (*a*) and (*c*). The black dashed lines in (*b*) and (*c*) serve as visual guides. For better comparison, the examined multi-XPR structure with up/down asymmetry from the bolometer tomography ($t = 6.2$ s) is horizontally mirrored and inserted in (*b*).

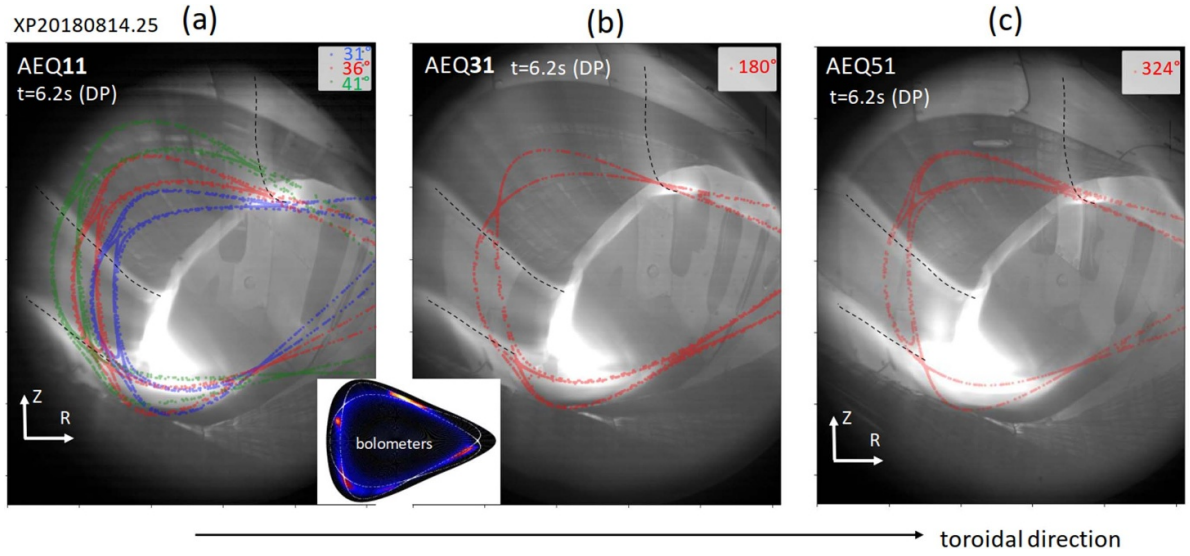

Figure 11. Images from video cameras observing the plasma in the DP phase of XP25 ($t = 6.2$ s) in different toroidal modules: (*a*) camera AEQ11 in M1, (*b*) camera AEQ31 in M3, and (*c*) camera AEQ51 in M5. In these camera images, the brightest areas from the divertor region are at the bottom. All cameras capture similar radiation patterns with multiple intense radiation bands (as indicated by the black dashed lines) that follow the toroidal field periodicity. The Poincaré plots for selected cross-sections at $\phi = 31^\circ$ (blue), 36° (red), and 41° (green) are overlaid in (*a*), while only the triangular cross-section ($\phi = 180^\circ$ and 324°) is overlaid in (*b*) and (*c*). For reference, the bolometer tomography image from figure 6(*d*) is included as an inset.

trace the field lines helically throughout the entire W7-X toroidal turn—has been ruled out. This hypothesis was based on the fact that X-lines follow the rotational transform at the LCFS ($\iota = 5/5$ for the SDC), resulting in a poloidal shift of $\Delta\theta = 72^\circ$ for each toroidal displacement of $\Delta\phi = 72^\circ$ (i.e. one field period). These helical radiation bands near X-points with poloidal asymmetry, caused by carbon impurities, were also observed in W7-AS with visible cameras [23] and in LHD based on spectroscopic measurements [26].

4. Examination of reversed field experiments

To determine whether the observed up/down asymmetry is influenced by drift effects, magnetic field reversal experiments are necessary. If drift mechanisms—such as $\mathbf{E} \times \mathbf{B}$ drift—significantly impact cross-field impurity transport, these experiments would invert the impurity radiation asymmetry. Such reversals have been observed in previous bolometer measurements before W7-X wall boronization, when radiation was dominated by oxygen [38].

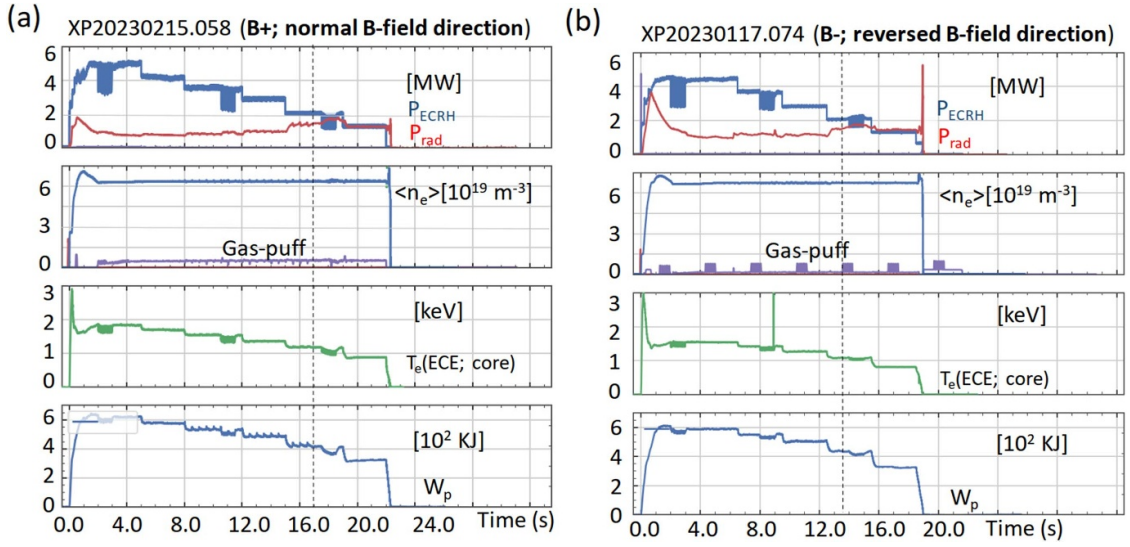

Figure 12. The key parameters in experiments with ECRH power reduction in normal (*a*) and reversed (*b*) field direction. Plasma detachment (signaled by high $f_{\rm rad}$) are reached in the later phase for low power steps (2 MW; 1 MW). The vertical dashed lines are the time points for examination of the field direction effect driven by drift on the up/down asymmetry in the multi-XPR structure in the DP phase ($f_{\rm rad} = 0.7$). Note that the $P_{\rm rad\_2D}$ values from the bolometer tomography are not displayed as they are very close to the presented $P_{\rm rad}$ values from the HBC measurements.

As of the completion of this work, density ramp experiments at fixed ECRH power in the reversed field direction have not yet been conducted. Two experiments—XP20230215.058 (XP58) and XP20230117.074 (XP74)—involving a stepwise reduction of ECRH power ($P_{\rm ECRH}$ ranges from ∼5 MW to ∼1.5 MW) in normal and reversed field directions, respectively, are analyzed.

Figures 12(*a*) and (*b*) summarizes the key plasma parameters of XP58 and XP74, including the values of $P_{\rm ECRH}$, the radiated power loss $P_{\rm rad}$ (from the HBC measurements), the line-averaged density $<n_{\rm e}>$, the plasma stored energy W_p and the electron temperature from the ECE diagnostic [73]. In both plasmas, the DP phase occurs at $f_{\rm rad} \sim 0.7$ (similar to figure 6(*c*) for XP25) at 2 MW ECRH power levels. At the last stage ($P_{\rm ECRH}$ ∼1.5 MW), the plasma enters the deep DP phase ($f_{\rm rad}$ ∼1). The value of $<n_{\rm e}>$ in these phases is fixed and is $\sim 6.0 \times 10^{19}$ m^{-3} in XP58 and $\sim 6.7 \times 10^{19}$ m^{-3} in XP74. Data analysis shows that the power fractions of the heating power in the SOL, and the radiated power fractions in both the core and SOL follow a similar trend with increasing $f_{\rm rad}$ as observed in XP25 (see figure 8(*b*)). This reconfirms that the radiation fraction $f_{\rm rad}$ determines the detachment process, regardless of whether it is triggered by a density lamp or an ECRH power reduction.

Figures 13(*a*) and (*b*) show the 2D radiation patterns for the DP phase with $f_{\rm rad} \sim 0.7$ obtained by the bolometer tomography at $t = 17.0$ s in XP58 and at $t = 13.5$ s in XP74. The corresponding video images with the representative camera AEQ40 are shown in figures 13(*c*) and (*d*). The results at the last stage in the deep DP-phase show less up/down asymmetry (similar to those in XP25 (figure 6(*f*)) and are not shown. For easy comparison, the bolometer results are mirrored horizontally.

It can be seen that (1) in the normal field direction, both the bolometer tomography and video images closely resemble the observations in the DP phase in XP25 (see e.g. figure 6(*c*)). They reproduce the multi-XPR structure—intense radiation around X2, X3 and X4—in the triangular cross-sections and show the helical band structure in the toroidal direction. The degree of the up/down asymmetry between the brightest X2 and its counterpart X5 is comparable to that in XP25. (2) In the reverse field direction, the multi-XPR structure persists in the triangular cross-section, but now the most intense XPR occurs near the lower X5, while the radiation around the upper X2 diminishes, i.e. the asymmetry flips. This is consistently shown by the bolometer and the video diagnostics (see figures 13(*b*) and (*d*)), and the video camera again shows the toroidal extension of this multi-XPR structure.

It should be noted that the intense radiation zone in the lower is5 (around the O point; in contrast to its counterpart is1) in the normal field case (figure 13(*a*)) is reversed in the upper is1 in the reversed field case (figure 13(*b*)), which is another example of the reversal of the up/down asymmetry. However, this effect is not clearly visible in the video image (figure 13(*d*)), which is probably due to the weaker intensity in visible light. Moreover, the asymmetric pattern inside is3 does not completely reverse when comparing figures 13(*a*) and (*b*), with the asymmetry degree being lower after field reversal. See section 5.2 for discussion.

Both diagnostics consistently capture the up/down asymmetry of the investigated XPR around X2 and X5, as well as its dependence on the magnetic field direction, despite minor differences in the observed patterns (e.g. near X4), which may arise from variations in spectral response of the two systems. These results suggest that drifts, such as the $\mathbf{E} \times \mathbf{B}$ drift, play a significant role in impurity transport and asymmetry formation.

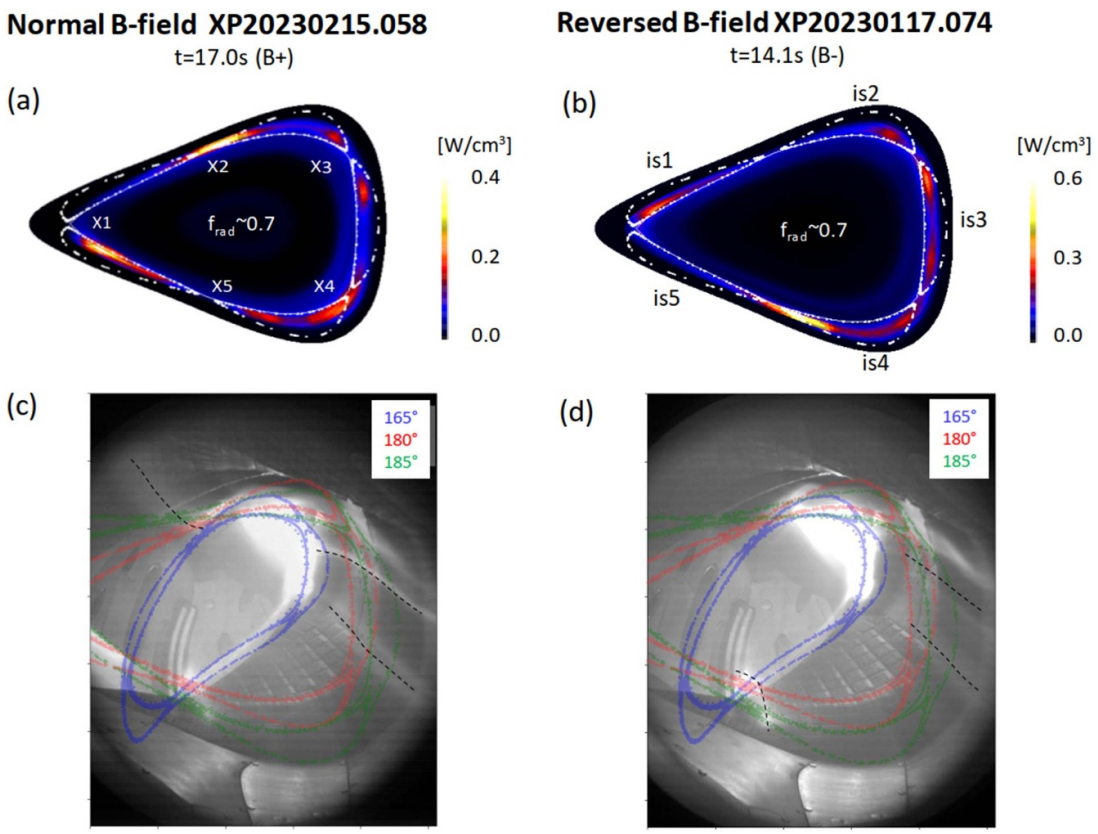

Figure 13. (*a*) and (*b*) 2D radiation distribution with a multi-XPR structure obtained by bolometer tomography for the normal field direction (XP58: 2 MW ECRH, $f_{\mathrm{rad}} = 0.7$, $<n_{\mathrm{e}}> 6.0 \times 10^{19}$ m^{-3}) and the reversed field direction (XP74: 2 MW ECRH, $f_{\mathrm{rad}} = 0.7$, $<n_{\mathrm{e}}>$ 6.7×10^{19} m^{-3}), showing the displacement of the strongest XPR from the upper X2 to the lower X5, exhibiting reversed asymmetry. (*c*) and (*d*) Video images from camera AEQ40 at the same time points for XP58 (*c*) and XP74 (*d*), confirming the major findings from bolometer tomography. For direct comparison, the bolometer results are horizontally flipped (inboard side on the right). Additionally, Poincaré plots for selected cross-sections at $\phi = 165°$ (blue), 180° (red), and 185° (green) are superimposed on the video images. The five X-points are labeled X1 to X5 in (*a*), while the five islands are labeled is1 to is5 in (*b*).

5. Comparisons of experimental results with 3D modeling and discussions on E × B drift effects on impurity transport and radiation asymmetry

So far, 3D modeling with the EMC3-Eirene code has been used to study plasma physics in the inherently 3D SOL of stellarators [74, 75] by combining a 3D fluid model for plasma transport with kinetic Monte Carlo modeling for neutral particle transport at the plasma boundary [41]. The current version does not take drift effects into account. The experimental example shown in section 3.2 was also selected in [10] to illustrate the most important aspects of plasma detachment in W7-X. The 2D radiation distributions shown there refer to the bean-shaped cross-section, which makes a direct comparison with the bolometer results difficult. In the following, we first present the modeling results in the triangular cross section. The deviation from the bolometer results allows us to gain insights into how drift can influence the radiation symmetry.

5.1. EMC3-Eirene simulations

The simulations of carbon impurity radiation are performed under the same experimental conditions as in XP25. Input parameters include the magnetic configuration for the vacuum field (SDC) and a total power of 5 MW in the computational domain ($\rho = r/a > 0.8$; 10% less than the ~5.5 MW ECRH port power), accounting for finite absorption of ECRH power and impurity radiation in the confinement region within $r/a < 0.8$.

This power is divided equally between electron and ion channels. The simulation assumes stellarator symmetry, meaning only one-tenth of the device is modeled—from a bean-shaped cross-section to an adjacent triangular cross-section. Carbon is considered as the only radiating impurity. The fluid model for impurities incorporates classical convection driven by the parallel temperature gradient $\nabla_{//} T_{\mathrm{e}}$ and $\nabla_{//} T_{\mathrm{i}}$ (thermal force) and friction due to collisions with the main ions, as well as an anomalous diffusion process perpendicular to the magnetic field. The diffusivity is set to $D = 0.5$ m^2 s^{-1} for both hydrogen and carbon. The thermal conductivities χ_{e} and χ_{i} for electrons and ions are set to 0.75 m^2 s^{-1}. The choice of these cross-field transport coefficients is a compromise obtained by fitting results of various local diagnostics, including IR-cameras, LPs, H_α-cameras, and Thomson scattering. Further details can be found in [10], where the same experimental example is used to explore the underlying physics of plasma detachment.

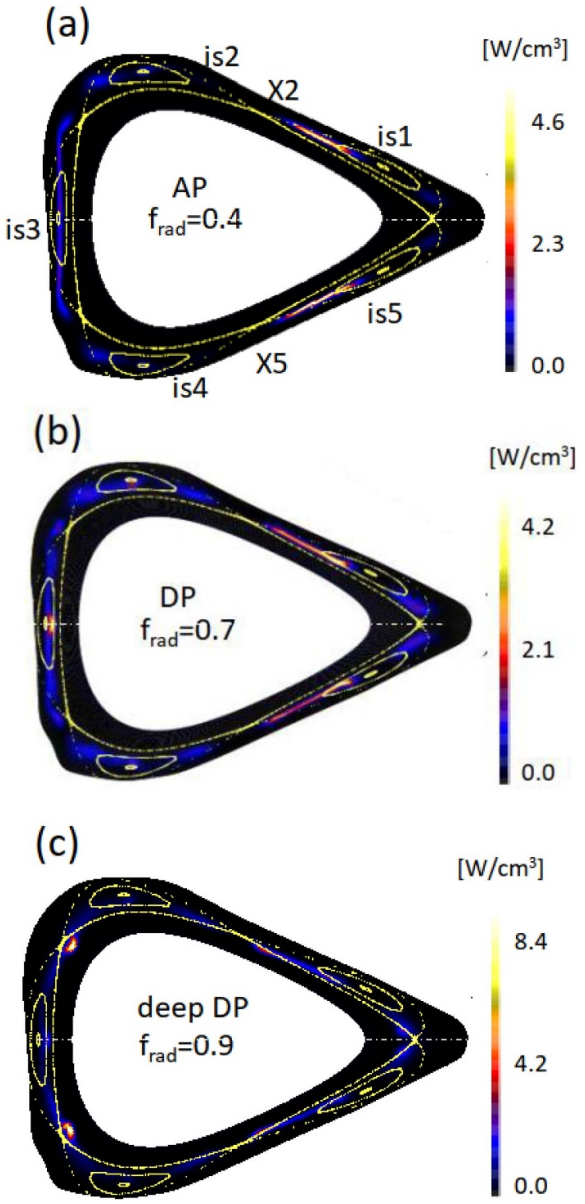

Figure 14. The 2D radiation patterns of carbon impurity obtained by 3D modeling with EMC3-Eirene code under plasma conditions corresponding to the AP (*a*), DP (*b*) and deep DP (*c*) phases in XP25 with $f_{\rm rad} = 0.4$, 0.7 and 0.9, respectively.

The results for the AP phase ($f_{\rm rad} = 0.4$, $<n_{\rm e}>0.75 \times 10^{20}$ m^{-3}), DP phase ($f_{\rm rad} = 0.7$, $<n_{\rm e}>0.8 \times 10^{20}$ m^{-3}) and deep DP phase ($f_{\rm rad} = 0.9$, $<n_{\rm e}>0.9 \times 10^{20}$ m^{-3}) in the triangular cross-section are shown in figures 14(*a*)–(*c*), respectively. Those for the bean-shaped plane can be found in figure 19(*a*) of [10]. It can be seen that the simulated 2D radiation patterns, $\varepsilon(r,\theta,)$, exhibit an overall up/down symmetry, following $\varepsilon(r,\theta,) = \varepsilon(r,-\theta)$ (θ = 0–180° with $\theta = 0$ at the X-point (X1) at the tip side), which aligns with the magnetic topology. Comparing these simulations with the bolometer results in Figure 6(*a*), (*c*) and (*f*), the following common trends are observed:

– AP phase: The radiation is localized near regions with shorter connection lengths ($L_{\rm c} < 35$ m) (see figure 3(*a*)).
– DP phase: the radiation shifts radially inward and simultaneously poloidally toward the X-points (e.g. X1, X2 and X5) due to flux surface expansion near the X-points [72].
– Deep DP phase: two intense radiation zones appear near the two X-points on the inboard side (X3 and X4), which is related to the increased density of neutrals that have a longer penetration length (∼several cm, comparable to the island width). A large part of the radiation is located within the LCFS, which is evident from the radiation patterns near X3 and X4. This result is very similar to the experimental results in figure 6(*f*). In these radiation zones the plasma is cold and dense, and around the X-points the electron temperature is only a few eV at a plasma density of $\sim 10^{20}$ m^{-3} (see figure 7 in [68]).

However, the up/down asymmetry observed by the bolometer tomography (figures 6(*a*)–(*d*)) is not reproduced, which is also not expected.

5.2. Discussions on the impact of the E × B drift on carbon impurity transport and radiation asymmetry in the SOL

The carbon impurity emissivity, $\varepsilon_{\rm rad}$, is given by

$$\varepsilon_{\rm rad} = n_{\rm e} n_z L_{z,} \tag{2}$$

where $n_{\rm e}$ is the plasma density, n_z is the impurity density, and L_z is the radiative loss coefficient, which depends strongly on electron temperature $T_{\rm e}$ [76]. In corona equilibrium, L_z peaks at $T_{\rm e} \approx 8$ eV (hereafter called effective radiation temperature $T_{\rm rad}$). Due to transport and CX processes, the value of $T_{\rm rad}$ may shift above 10 eV (see also simulation results using EMC3-Eirene code; figure 6 [72]) as these processes change the abundance of impurity ions [76]. In the SOL plasmas studied the main carbon ions are those with low charge states Z = 1–3 (CII, CIII, and CIV). The observed up/down asymmetry of emissivity normally reflects the asymmetric distribution of these carbon ion impurities.

In this discussion, the effects of $\mathbf{E} \times \mathbf{B}$ drift for the normal magnetic field direction on the impurity transport in the DP phase (except for the deep DP phase) are investigated. A simplified model is shown schematically in figures 15(*a*) and (*b*) for the selected upper and lower SOL regions, which mainly consider the frictions between impurity and main ions (driving impurity ions downstream) and the poloidal component of $\mathbf{E} \times \mathbf{B}$ drift (driving a clockwise drift flow around the O-point of the islands). These SOL regions imitate is2 and is4 (partially is3) in the triangular cross-section bounded by TSRs or the magnetic islands intersecting divertor targets that magnetically connecting is2–is4 (i.e. downstream source locations). The considerations are as follows.

5.2.1. The role of friction force in impurity transport. EMC3-Eirene simulations have shown that the friction force dominates over the thermal force in determining the parallel

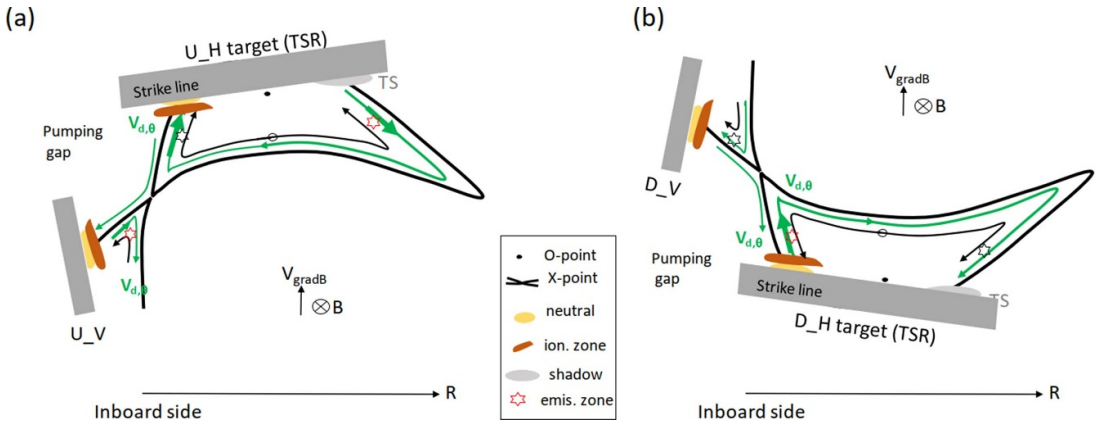

Figure 15. Schematic illustration of the poloidal drift velocity (green arrows) of charged particles and the projection of impurity ion flow (black arrows) in a friction-dominant case without considering drifts, for the selected upper (*a*) and lower (*b*) SOL in W7-X under the normal magnetic field direction. The grad-B drift, which induces an upward drift velocity, is also indicated. The horizontal and vertical target plates (or TSRs) are shown as grey bars and labeled U_H and U_V for the upper and D_H and D_V for the lower. The neutral population zones (yellow ovals, near the targets) and ionizations zone (brown ovals) are depicted. Regions marked with red stars indicate areas where the poloidal drift is directed toward the LCFS, while black stars mark regions where the poloidal drift is directed toward the TSR.

transport of impurities in the W7-X SOL. As a result, the parallel plasma flow ($V_{i\|}$) drives impurities downstream towards targets or TSRs ($V_{z\|} \approx V_{i\|}$) [8], rather than pulling them upstream toward high-temperature regions, as the thermal force would do. The predicted parallel counter-streaming flow of impurity ions CIII has been observed experimentally in W7-X using CIS diagnostics [77]. The flow projections on both sides of the island SOL, i.e. a 'net' impurity flow $V_{Z,f} = -\Theta V_{Z\|}$ ($\Theta \approx 0.001$, representing the internal pitch of the field lines), are both directed towards the divertor targets (i.e. downstream; $V_{Z,f} < 0$). Figures 15(*a*) and (*b*) schematically illustrate this impurity flow $V_{Z,f}$ (without considering the drift) in the upper and lower island SOL. The stagnation point of the parallel flow projection (in black arrows), where $V_{i\|} = 0$ corresponding to pressure maximum in the island SOL with zero poloidal pressure-gradient-force, is only roughly marked (in black circles). Its position may shift poloidally due to drift (clockwise about the O-point), but for the studied high-density plasmas it is small [49] and thus not emphasized.

Without considering $\mathbf{E} \times \mathbf{B}$ drifts, the impurity density in the island SOL ($n_{Z\mathrm{S}}$) is determined by the parallel-to-perpendicular transport ratio $\frac{V_{Z,f}}{D} = -\frac{\Theta V_{Z\|}}{D}$, where D is the diffusivity. In source-free regions, it can be derived from the 1D continuity equation (see equation (9) in [8]). For the target-released carbon impurities, it follows [8]:

$$n_{ZS} = n_{Zd}\exp\left(\int_0^x \frac{-\Theta V_{Z\|}}{D}\mathrm{d}x\right), \tag{3}$$

where n_{ZS} is the impurity density at a given location x (distance from the downstream source), and n_{Zd} is the downstream impurity density (near the targets or TSRs). This equation shows that a higher value of $\Theta V_{Z\|}$ leads to a lower impurity density in the SOL.

5.2.2. The poloidal E × B drift and its impact on impurity asymmetry. Of all drift mechanisms, the $\mathbf{E} \times \mathbf{B}$ drift is considered as the most effective for deflecting charged particles from their original trajectories aligned with the magnetic field. Being independent of charge and mass, it affects impurity ions, main ions, and electrons equally. Its effects on the W7-X SOL plasma in the 'low-iota' magnetic configuration were mainly investigated for low-density plasmas [47, 49]. A similar approach can be applied here to the SDC to determine its radial and poloidal components. (1) The radial drift ($V_{\mathrm{d,r}} = E_\theta/B$), which is determined by the poloidal electric field E_θ (directing from the X-point to the divertor target (or TSR) along the separatrix), flows from the PFR near an X-point into the island SOL and from the island SOL into the PFR near another X-point. (2) The poloidal drift $V_{\mathrm{d},\theta}$ is determined by the radial electric field E_r, which is influenced by the radial variation of plasma potential depending on the T_e distribution [43]. In most phases of the SOL plasma studied (XP25 being representative), T_e is highest at the inner separatrix (LCFS) and decreases radially outwards. Its value at the O-point is normally low, which is due to the fact that there is no direct heat deposition in this region and the perpendicular heat flux from the core plasma into this domain is low. In the PFR, T_e also decreases radially outward but is higher at the X-points and the LCFS [78]. As a result, within the islands, E_r points toward the O-point, while in the PFR, it points away from the LCFS. For the normal W7-X field direction, $V_{\mathrm{d},\theta}$ is clockwise about the O-point inside each island and reverses its direction across the island SOL-PFR boundary (see the green arrows in figures 15(*a*) and (*b*)).

Based on the experimental observations and numerical modeling results in stellarators [46, 47, 49], poloidal drift plays a dominant role in governing the asymmetry of charged particles, so we focus on its effects. Further consideration of the radial $\mathbf{E} \times \mathbf{B}$ drift component will be a topic for future work. The grad-B drift is charge-dependent and induces a plasma current, it influences particle and heat transport like

the radial $\mathbf{E} \times \mathbf{B}$ drift, which is also not further investigated in this work. Note that this simplified model of poloidal drift assumes that the T_e-value around the O-point is a minimum in the island. This is true for the AP and DP phases in XP25, as the T_e-values at the inner separatrix (LCFS; see figure 4(d)) and near the strike lines are clearly higher than near the O-point (see the LP measurements in figure 19(*a*)). However, at the transition from the DP to the deep DP phase, the difference becomes small, and this model is then not applicable. This discussion also does not apply to the deep DP phase, where the up/down asymmetry is much smaller.

We further assume that the impurity and main ions experience an equivalent poloidal $\mathbf{E} \times \mathbf{B}$ drift and are tightly coupled to each other due to high collisions. It can be seen (as shown in figures 15(*a*) and (*b*)) that the poloidal drift flow in the left and right partitions of the upper and lower island SOL is either parallel ($V_d = -V_{d,} < 0$, directed towards targets or TSR) or antiparallel ($V_d = V_{d,} > 0$, directed towards LCFS) to the impurity flow. Replacing $-\Theta V_{z\|}$ by an effective flow velocity $-\Theta V_{Z\|,\mathrm{eff}} = -\Theta V_{z\|} + V_d$ in equation (3) gives the following result:

$$n_{ZS} = n_{Zd} \exp\left(\int_0^x \frac{-\Theta V_{Z\|} + V_d}{D} \mathrm{d}x \right). \tag{4}$$

It indicates that (1) in regions where $V_d > 0$ (hereafter: upstream drift, e.g. right partition in the upper SOL, left partition in the lower SOL, marked by red stars in figures 15(*a*) and (*b*)), the impurity density increases; (2) in regions where $V_d < 0$ (hereafter: downstream drift, e.g. left partition in the upper SOL, right partition in the lower SOL, marked by black stars in figures 15(*a*) and (*b*)), the impurity density decreases.

Defining a normalized drift velocity as $V^*_{d,} = \frac{V_{d,}}{D}$ (assuming it remains constant), the ratio of impurity density γ_Z between the island regions with upstream drift and the island region with downstream drift scales as

$$\gamma_Z \propto \mathrm{e}^{\left(2\Delta x V^*_{d,\theta}\right)} \gamma_{Zd}, \tag{5}$$

where γ_{Zd} represents the ratio of the corresponding downstream impurity sources. This indicates that both the factor of $\Delta x V^*_{d,\theta}$ and γ_{Zd} play a role in influencing impurity asymmetry.

In the DP phase, the emission zone shifts with increasing f_{rad} from the TSR to the LCFS (with a maximum $\Delta x \approx 5.0$ cm) (see figure 8(left)). Assuming $D = 0.5$ m^2 s^{-1} and $V_d = 30$ m s^{-1}, the estimated $\mathrm{e}^{\left(2\Delta x V^*_{d,\theta}\right)}$ for $\Delta x = 5.0$ cm yields a value of $\sim$150. This shows the influence of the emission zone shift on gaining the asymmetry degree. Since no measurements of V_d are available for the plasmas studied, we have used here a conservative small value for V_d based on previous studies of the W7-X-SOL plasma, ranging from a few tens of m/s to $\sim$1 km s^{-1} and decreasing with increasing density and f_{rad} [47, 49].

This large factor (which is roughly due to the simplified drift model) underlines the important role of the normalized poloidal drift velocity in causing the impurity asymmetry. This also sheds light on the question of why the degree of asymmetry in the radiation intensity around X2 and X5 (figures 5(*b*)–(*d*)) increases with increasing f_{rad}. It is to be expected that the background plasma density can additively influence the radiation asymmetry, since regions with higher radiation intensity have a relatively lower T_e value (due to radiation cooling) and thus a higher electron density, which promotes radiation intensity asymmetry.

Furthermore, we intend to apply this model to explain the up/down asymmetry in the radiation pattern at the onset of the DP phase, which corresponds to $\Delta x \approx 0$ (i.e. $\mathrm{e}^{\left(\Delta x V^*_{d,\theta}\right)} \approx 1$ in equation (5)), for which the asymmetry of the downstream impurity sources (γ_{Zd}) is the determined. These downstream impurity sources, including neutral particles (C atoms from physical sputtering and hydrocarbons from chemical sputtering) and ionization zones (CI ionization energy $\sim$11.3 eV), are also depicted in figures 15(*a*) and (*b*) near the strike lines. They are on the inboard side (near the pumping gap) for the SDC. Since the neutral penetration length λ_0 is sensitive to the electron temperature and density in the SOL, its value increases with increasing f_{rad}, and these zones can cross the magnetic island as in the deep DP phase [10]. It can be seen that the poloidal drift in the left partition of the upper island shifts the CII ions towards the divertor targets (figure 15(*a*)) and thus promotes recombination. Conversely, the drift in the left partition of the lower island shifts the CII ions towards the LCFS, where T_e is higher, promoting excitation and further ionization to CIII. As a result, the impurity ions are distributed asymmetrically, with the impurity content being higher in the lower left island partition ($\gamma_{Zd} > 1$). Consequently, the left-hand region in the lower island SOL radiates more strongly than the upper island SOL, which qualitatively explain the up/down asymmetry in the impurity radiation pattern in figure 6(*b*). It should be noted that a large variation of γ_{Zd} during detachment proceeding can offset or counteract the effect of the radiation zone shift (Δx). This corresponds to the radiation asymmetry in the left regions of the upper and lower islands (is2 and is4) (see black circles in figure 7(*b*)), which remains almost unchanged with increasing f_{rad} despite the radiation layer shift. The influence of the variation of γ_{Zd} on the radiation asymmetry in the right regions (X2 and X5) does not seem to be determined.

In addition, the radiation asymmetry observed in is3 (figures 6(*a*)–(*d*)) is believed to be also due to the poloidal drift effect, as the drift flow in the region with the higher emissivity is directed towards the LCFS (upstream drift; see figure 15(*a*)), which is consistent with the model predictions for higher impurity content there.

Remarks. As already mentioned, the $\mathbf{E} \times \mathbf{B}$ drift leads to an asymmetry in the particle flux and heat load on the divertor targets, which has already been studied in 'low-iota' plasmas in W7-X and other devices. These asymmetries lead to an asymmetry in the impurity source (e.g. CII emission) generated by sputtering processes, which closely relates to the up/down asymmetry in the radiation pattern in the AP phases (see figure 6(*a*)). A detailed investigation of the AP phase is beyond the scope of this work. More results about these edge parameters can be found in appendix B.

6. Summary

In W7-X, stable plasma detachment in ECRH hydrogen plasmas is routinely achieved with the SDC, where intrinsic carbon is the main impurity species. Detachment is characterized by a high radiation fraction $f_{\rm rad}$, leading to a significant reduction in both heat load and particle flux on divertor targets. This regime can be reached via density ramping or heating power reduction. Generally, after onset of the DP phase ($f_{\rm rad}$ >0.6), the bolometer results shows that the radiation zones shift radially inwards from the region near the TSR in the SOL to the LCFS, with a concomitant poloidal shift to the X-points as $f_{\rm rad}$ increases. A clear decrease in the edge temperature and an increase in radiation within the LCFS (up to 60%) are observed. These basic features of detachment are consistent with EMC3-Eirene modeling results [10], and the intense X-point radiation (XPR) is understood as an effect of flux expansion [72].

The main findings of this study are as follows:

i. In the DP phase ($f_{\rm rad} = 0.6$–0.9), the 2D radiation profiles from the bolometer tomography have revealed a multi-XPR structure featuring an up/down asymmetry in the triangular plasma cross-section, which possesses an up/down symmetric magnetic topology. The video cameras confirm this asymmetry and further show that the multi-XPR exhibits a multi-band structure helically following the trajectory of the X-points (similar to the carbon radiation character in W7-AS [23] and LHD [26]) and retaining the field periodicity of W7-X. Field reversal experiments confirm that the brightest XPR shifts between the upper and lower SOL regions in response to magnetic field direction, suggesting the key role of $\mathbf{E} \times \mathbf{B}$ drift in impurity transport. This up/down asymmetry cannot be explained by the 3D modeling with EMC3-Eirene, which does not account for drifts. At high radiation level ($f_{\rm rad} > 0.9$; deep DP), the radiation zones shift towards the two X-points at the inboard side, and the up/down asymmetry is reduced significantly.
ii. A simplified model is applied mainly considering the influence of the poloidal $\mathbf{E} \times \mathbf{B}$ drift $V_{\rm d}$ on the impurity flow in the island SOL, which is otherwise mainly determined by friction due to collisions with the main ions. It indicates that downstream drift towards the target or TSR ($V_{\rm d} < 0$) enhances the effective impurity flow, decreasing the impurity content, while upstream drift towards the LCFS ($V_{\rm d} > 0$) decreases the effective impurity flow, enhancing the impurity content. On this basis, the poloidal drift (clockwise around the O-point in the island SOL for the normal field direction) potentially leads to an up/down asymmetry of the impurity density in the island SOL despite the symmetry magnetic topology.
iii. The up/down asymmetry appeared in the multi-XPR structure in the DP phase is qualitatively explained: the normalized $V_{\rm d}$ to impurity diffusivity (i.e. $V_{\rm d}/D$) and the radial distance of the radiation zone to the impurity source determine the asymmetry degree, while the downstream source—which is also influenced by the poloidal drift—further adjusts the degree. This asymmetry, however, almost disappears in the deep DP phase, which results in an almost homogeneously thermal removal from all the divertor targets.

The study establishes an experimental basis for future modeling improvements, particularly for drift effects in impurity transport. In the future, the main features of our model in dealing the radiation asymmetry should be further verified experimentally in conjunction with boundary plasma parameters [78] and electric field measurements [79] in various magnetic configurations.

A detailed analysis of the radiation asymmetry in the AP phase is planned for the next work.

Acknowledgments

The author D. Zhang thanks Professor B. Peterson (NIFS, Japan) and Dr G. Wurden (LANL, USA) for general discussions on the bolometer measurements, Dr L Rudischhauser for discussions on Langmuir probe measurements, and Dr A. Pavone for performing Gaussian process fits to the Thomson scattering data and providing the $Z_{\rm eff}$ values. This work has been carried out within the framework of the EUROfusion Consortium, funded by the European Union via the Euratom Research and Training Programme (Grant Agreement No 101052200—EUROfusion). Views and opinions expressed are however those of the author(s) only and do not necessarily reflect those of the European Union or the European Commission. Neither the European Union nor the European Commission can be held responsible for them.

Appendix A. Chord brightness-profile evolution in the detachment regime in XP25

The chord brightness profiles from both HBC and VBC used as inputs for performing the bolometer tomography are presented, taking several time points (e.g. the same as in figure 6) after the onset of DP for showing its evolution. The chord brightness of bolometer channel l is derived from the power it measures, P_l, normalized to a geometry factor K_l that is proportional to the length of the LoS through the entire plasma volume and the camera Etendu, i.e. $<\varepsilon_l> P_l/k_l$ [38]. Figures 16(a) and (b) illustrates the $<\varepsilon_l>$-profile evolution for the HBC ($t = 5.5$–6.5 s), and those for the VBC are shown in figures 16(c) and (d).

– For the HBC, the lower edge channels (ch25-27) detect much stronger plasma radiation at DP onset ($t = 5.5$ s). As $f_{\rm rad}$ increases (with time), upper SOL brightness intensifies, with ch5 showing the most significant rise. Channels 13–14, spanning both core plasma and SOL islands, exhibit enhanced brightness, indicative of island radiation. Note that ch6 and ch27 are the channels viewing the upper and lower LCFS.

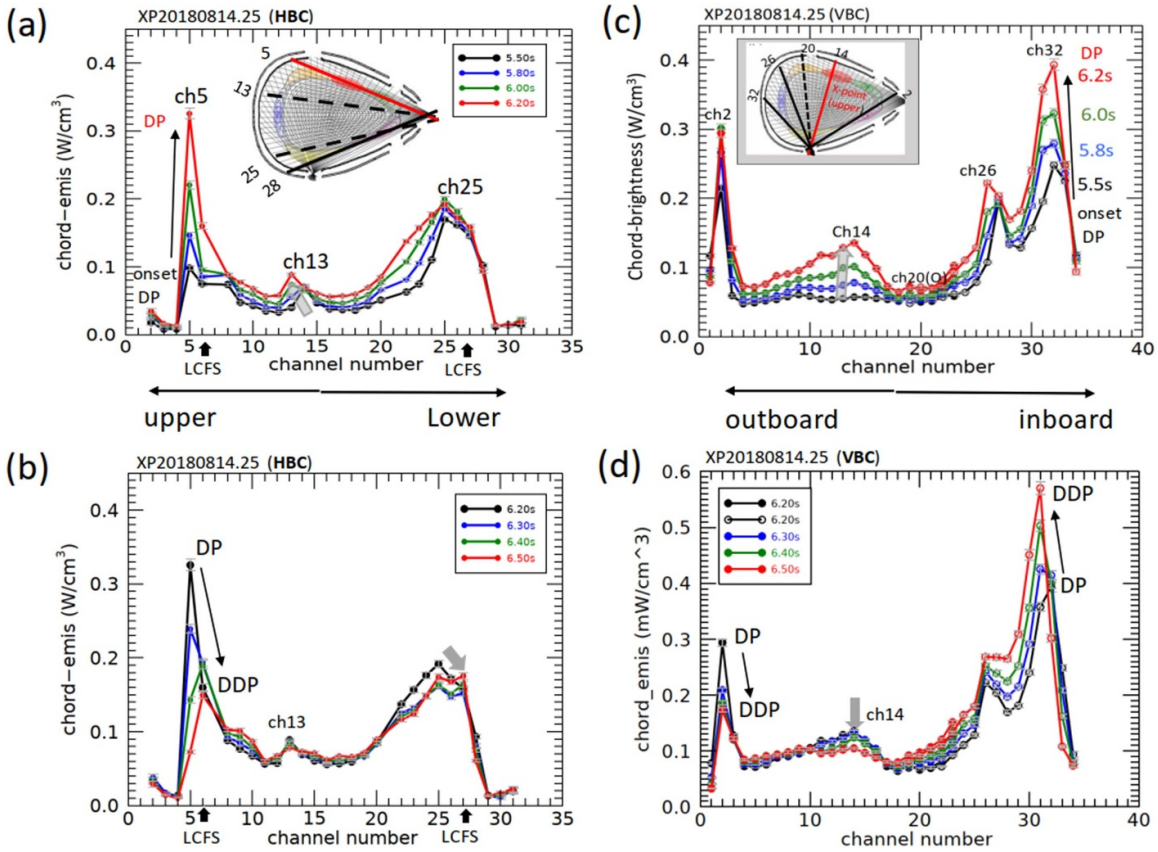

Figure 16. Time evolution of the chord-brightness profiles of the HBC (*a*), (*b*) and the VBC (*c*), (*d*) in the DP phase ($t = 5.5$–6.2 s) and during the transition from DP to deep DP phase ($t = 6.2$–6.5 s, labeled DDP), demonstrating the formation of the multi-XPR structure and its dynamics with increasing density and f_{rad}. Insets show the LoS in the HBC and VBC near the X-points, overlaid with Poincaré plots for the SDC.

– For the VBC, the channels viewing plasma region near the X-points (such as ch2, ch14, ch26, ch32) show increasing brightness after the onset of the DP phase. The signal of ch14 (viewing the upper X-point) peaks at $t \sim 6.2$ s. For $t > 6.2$ s, the chord-brightness decreases, while inboard-side brightness strengthens. The resultant 2D radiation pattern (figures 8(*d*)–(*f*)) correspondingly shows the bright radiation around the two inboard X-points.

This analysis serves as an additional proof of the 2D radiation patterns from the bolometer tomography as shown in figures 6(*b*)–(*f*).

Appendix B. Additional boundary plasma diagnostic observations in XP25

Due to the 3D magnetic topology in the W7-X SOL, the heat flux on the divertor targets is usually not uniformly distributed as shown in figures 5(*a*) and (*b*). To gain insight into the up/down asymmetry of the heat load profiles and the resulting source of carbon impurities released, the temporal evolution of the heat flux and CII emission profiles at representative toroidal positions is investigated. These are located at the identical toroidal positions as the LP arrays (in M5 at $\phi = -63°$ on the upper target and $\phi = -81°$ on the lower targets), but on the divertor targets in M4, where the IR cameras (AEF41 and AEF40) to measure the heat flux and the visible light cameras (41B and 40B) to measure the CII emissions are all available.

Figures 17(*a*) and (*b*) show the temporal evolution of the heat flux profile on the upper and lower target plates in XP25, and the corresponding CII emission profiles in figures 17(*c*) and (*d*). The Y-axis is the distance from the pumping gap relative to the border of the target plates. The locations of the three LPs (8–10) near the strike lines (black dashed lines) are indicated. This strike line is located at a distance of $s = 13.5$ cm from the pumping gap, which corresponds to the ideal case of a vacuum-magnetic configuration [57], without considering the error field effect. The up/down asymmetry is clearly visible both in the peak values and in the profile width, with the degree of asymmetry varying with increasing f_{rad}.

(1) During the AP phase ($t = 2.0$ s–5.5 s; $f_{\mathrm{rad}} < 0.6$), the upper strike zone (high heat flux region) exhibits a higher peak heat load located ∼4 cm closer to the pumping gap than the lower one when comparing the strike zone boundary position (where the heat flux drops to ∼60% of the peak value; marked by white dashed lines). The upper profiles for both heat flux and CII emissions are narrower than the lower ones.

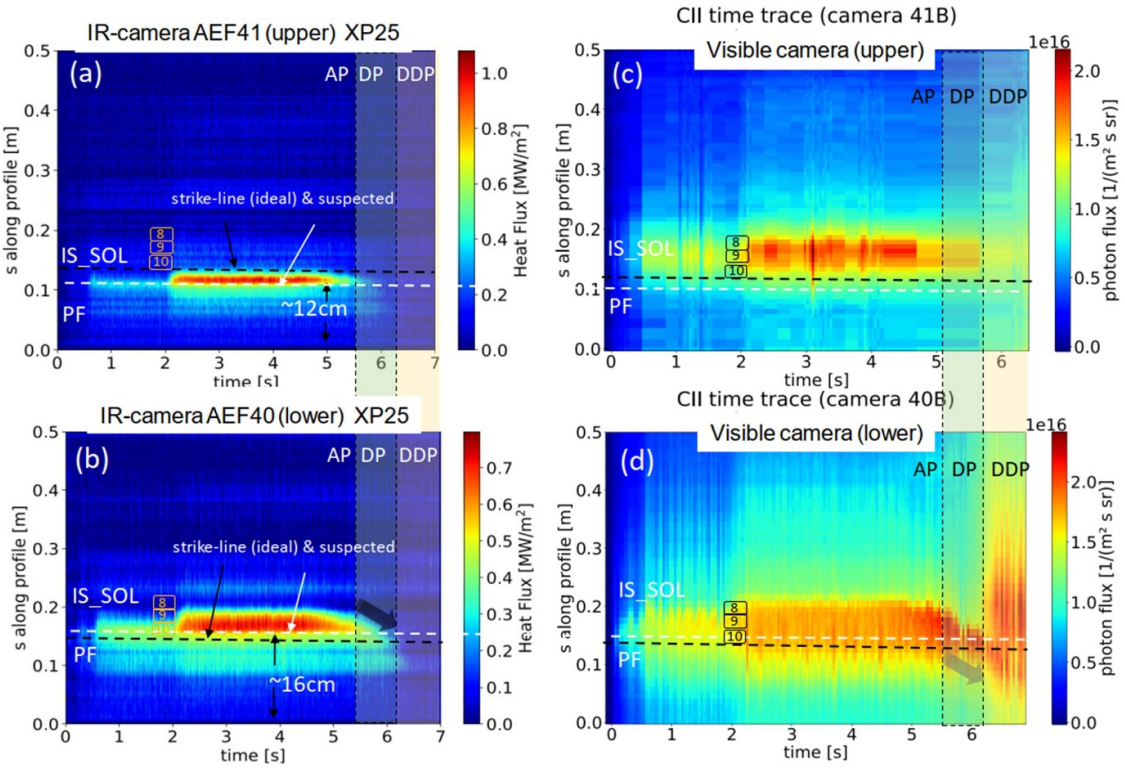

Figure 17. Time histories of the heat load profiles (*a*), (*b*) and the CII emission profiles (*c*), (*d*) on the upper (at $\phi = -63^\circ$–72°) and lower (at $\phi = -81^\circ$–72°) divertor targets in M4 for XP25. The black horizontal dashed lines represent the position of the 'vacuum' strike line at $s = 13.5$ cm, while the white dashed lines, drawn manually, mark the strike zone borders based on the heat load profiles. The plasma phases, including AP, DP and deep DP (labeled DDP), are indicated. Note that for $t > 4.0$ s in panel (*c*), the visible camera data points become sparse due to missing frames in the camera DAQ system in reaction to the overexposed frames.

(2) In the DP phase ($t > 5.5$ s; $f_{\mathrm{rad}} = 0.6$–0.9), the heat load on both the upper and lower targets decreases, but the lower target now receives a higher peak value, indicating a reversal of the asymmetry correlated with the asymmetry of the edge radiation (see figure 4(*f*)), which is due to the fact that higher radiative cooling in the upper SOL causes a lower temperature and thus a lower energy carried by the particles. The peak photon flux ($\sim 2.5 \times 10^{16}$ m^{-2}s^{-1}sr^{-1}) of the CII emission near the lower targets surpasses the upper one by a factor of $\sim$1.5 accompanied by an attenuation of CII emission in the upper SOL. This is likely due to poloidal drift, which shifts CII ions downstream in the upper island SOL, promoting recombination and it shifts the CII ions upstream towards the LCFS in the lower SOL, promoting excitation.

(3) In the deep DP phase ($t > 6.2$ s, $f_{\mathrm{rad}} \sim 1$; labeled DDP), the peak heat load drops by a factor of over 10 in both profiles, and the up/down asymmetry is not visible, indicating homogeneous thermal load removal. The CII ions are far away from the target (near the LCFS). The upper emissivity continues to decrease, while at the same time the lower profile becomes much broader and extends into the PF region (indicated by the gray arrow in figure 17(*d*)).

However, difficulties are encountered when trying to explain the strike zone location in the upper divertor target. Based on the simplified model in figure 15(*a*), it is expected that the stronger plasma-target interaction should be located in the island SOL, where the drift enhances the particle flux. This is not possible in the PFR, as shown in figure 17(*a*), where the drift should push the particles away from the upper targets. We suspect that error fields influence the actual position of the strike line.

In addition, the incomplete LP coverage of the strike zone makes a direct verification of the $\mathbf{E} \times \mathbf{B}$ model impossible. For completeness, the LP results are summarized here. Figures 18(*a*)–(*c*) shows the profile of the ion saturation current (J_s as a function of probe location R) of all upper and lower LPs in the AP, DP and deep DP phases in XP25. Almost all the lower probes (red) show a higher particle fluxes, with probes in the TSR (LP1-5), leading to a small impurity source asymmetry (γ_{Zd}; see section 5.2), consistent with the model prediction (as shown in green arrows in figure 15), while those from LP6-10 (monitoring the strike zone) are not expected, as the model predicts that poloidal drift causes a higher particle flux towards the upper target (rather towards the lower targets).

A closer look at the probe locations reveals that the upper LPs are located outside the actual strike zone in the upper target (see figure 17(*a*)), while the lower LPs remain within the lower strike zone. The complete displacement of the upper LPs from the upper strike zone explains why the average ion saturation current J_s of all upper LPs (see figure 4(*h*)) is significantly lower than that of the lower LPs.

The intense CII emission remains restricted to the upper island SOL, and the lower emission extends to some extent into the PF region. This main location of the emission

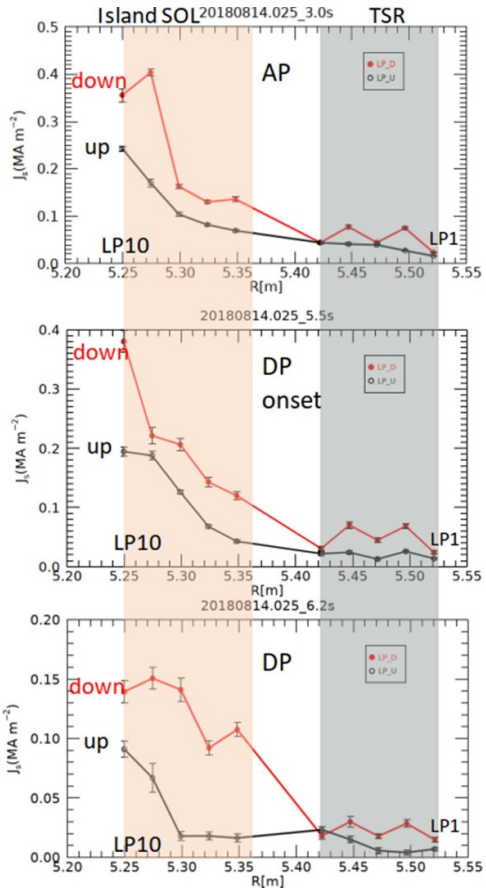

Figure 18. Evolution of the ion saturation current profile in the AP, DP and deep DP phases in XP25. The locations of the upper and lower probes are indicated based on the ideal SOL magnetic topology for SDC: LP1-5 are positioned in the TSR, while LP6-10 are in the island SO, with LP10 pairs being the closest to the ideal strike lines.

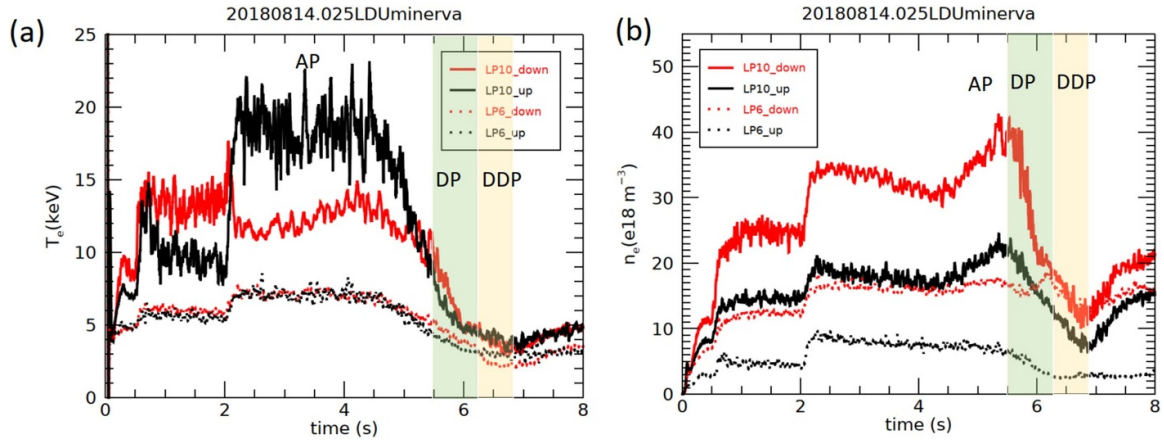

Figure 19. Time histories of the upper and lower LP10 (closest to the ideal vacuum strike lines) and LP6 (closest to the O-points) showing the evolution of the target temperature $T_{e,t}$ and density $n_{e,t}$ in the AP, DP and deep DP phases (5.5 MW ECRH; $t > 2.0$ s) in XP25. The locations of LP10 pair are schematically illustrated in figure 17.

zone (∼15 cm from the pumping gap) is confronted with a target temperature of $T_{e,t} \sim$ 12–14 eV, which is measured by the probes near the emission zones (e.g. LP9-10). Representatively, figures 18(*a*) and (*b*) show the time histories of the target parameters $T_{e,t}$ and $n_{e,t}$ measured with the LP10 pair. Since the upper and lower LP10 are located in different regions relative to the strike zones on the divertor targets, an up/down asymmetry is not directly accessible here either. It is noticeable that the deviation between the two values decreases after the onset of the DP phase. In particular, the two $T_{e,t}$ values are similar and decrease from ∼10.0 eV to ∼3.5 eV when the plasma enters the deep DP phase. This is consistent with the decrease in the asymmetry of the heat load in the DP phase, as shown in figures 17(*a*) and (*b*). In addition, figures 18(*a*) and

(*b*) also show the time histories of the target parameters in the regions near the O-points measured with the LP6 pair, which have lower values in the AP and DP phase than those of LP10 pairs, with small differences in the deep DP phase.

Further validation of the simplified $\mathbf{E} \times \mathbf{B}$ drift model for the plasmas in the SDC for these boundary parameters remains a task for future studies, particularly once error field correction is optimized and the spatial coverage of the LPs is improved.

ORCID iDs

D. Zhang 0000-0002-5800-4907
G. Cseh 0000-0003-4729-8070
Y. Gao 0000-0001-8576-0970
M. Jakubowski 0000-0002-6557-3497
T. Kremeyer 0000-0002-6383-944X
D.M. Kriete 0000-0002-3657-2911
G. Schlisio 0000-0002-5430-0645
G. Partesotti 0009-0008-9465-7885
V. Perseo 0000-0001-8473-9002
A. Alonso 0000-0001-6863-8578
S.A. Bozhenkov 0000-0003-4289-3532
Ch. Brandt 0000-0002-5455-4629
K.J. Brunner 0000-0002-0974-0457
B. Buttenschön 0000-0002-9830-9641
J. Geiger 0000-0003-4268-7480
L. Giannone 0000-0001-5611-200X
V. Haak 0000-0001-9158-5566
K.C. Hammond 0000-0002-1104-4434
K. Rahbarnia 0000-0002-5550-1801
T. Szepesi 0000-0002-8305-3858
V. Winters 0000-0001-8108-7774

References

[1] Matthews G. 1995 Plasma detachment from divertor targets and limiters *J. Nucl. Mater.* **220** 104–16
[2] Petrie T. *et al* 1997 Radiative divertor experiments in DIII-D with D2 injection *Nucl. Fusion* **37** 321
[3] Kallenbach A. *et al* 2015 Partial detachment of high power discharges in ASDEX Upgrade *Nucl. Fusion* **55** 053026
[4] Stangeby P. 2018 Basic physical processes and reduced models for plasma detachment *Plasma Phys. Control. Fusion* **60** 044022
[5] Krasheninnikov S. and Kukushkin A. 2017 Physics of ultimate detachment of a tokamak divertor plasma *J. Plasma Phys.* **83** 155830501
[6] Grigull P. *et al* 2001 First island divertor experiments on the W7-AS stellarator *Plasma Phys. Control. Fusion* **43** A175
[7] Wagner F. *et al* 2005 W7-AS: one step of the Wendelstein stellarator line *Phys. Plasmas* **12** 072509
[8] Feng Y., Sardei F., Grigull P., McCormick K., Kisslinger J. and Reiter D. 2006 Physics of island divertors as highlighted by the example of W7-AS *Nucl. Fusion* **46** 807
[9] Kobayashi M. *et al* 2010 Detachment stabilization with n/m= 1/1 resonant magnetic perturbation field applied to the stochastic magnetic boundary of the large helical device *Phys. Plasmas* **17** 056111
[10] Feng Y. *et al* 2021 Understanding detachment of the W7-X island divertor *Nucl. Fusion* **61** 086012
[11] Lipschultz B., LaBombard B., Marmar E.S., Pickrell M.M., Terry J.L., Watterson R. and Wolfe S.M. 1984 Marfe: an edge plasma phenomenon *Nucl. Fusion* **24** 977
[12] Mertens V. *et al* 1994 Experimental investigation of marfes and the density limit in the ASDEX upgrade *Plasma Phys. Control. Fusion* **36** 1307
[13] Oberkofler M. *et al* 2013 First nitrogen-seeding experiments in JET with the ITER-like Wall *J. Nucl. Mater.* **438** S258–61
[14] Reimold F., Wischmeier M., Bernert M., Potzel S., Kallenbach A., Müller H.W., Sieglin B. and Stroth U. 2015 Divertor studies in nitrogen induced completely detached H-modes in full tungsten ASDEX Upgrade *Nucl. Fusion* **55** 033004
[15] Bernert M. *et al* 2017 Power exhaust by SOL and pedestal radiation at ASDEX Upgrade and JET *Nucl. Mater. Energy* **12** 111–8
[16] Stroth U., Bernert M., Brida D., Cavedon M., Dux R., Huett E., Lunt T., Pan O., and Wischmeier M. (ASDEX Upgrade Team) 2022 Model for access and stability of the X-point radiator and the threshold for marfes in tokamak plasmas *Nucl. Fusion* **62** 076008
[17] Bernert M. *et al* 2020 X-point radiation, its control and an ELM suppressed radiating regime at the ASDEX Upgrade tokamak *Nucl. Fusion* **61** 024001
[18] Cavedon M. *et al* 2022 Experimental investigation of L-and H-mode detachment via the divertor Thomson scattering at ASDEX Upgrade *Nucl. Fusion* **62** 066027
[19] Hirsch M. *et al* 2008 Major results from the stellarator Wendelstein 7-AS *Plasma Phys. Control. Fusion* **50** 053001
[20] Komori A. *et al* 2009 Development of net-current free heliotron plasmas in the large helical device *Nucl. Fusion* **49** 104015
[21] Grigull P. *et al* 2003 Influence of magnetic field configurations on divertor plasma parameters in the W7-AS stellarator *J. Nucl. Mater.* **313** 1287–91
[22] Giannone L. *et al* 2003 Bolometer tomography at the density limit of the HDH mode in the W7-AS stellarator *Plasma Phys. Control. Fusion* **45** 1713
[23] Thomsen H., König R., Feng Y., Grigull P., Klinger T., McCormick K., Ramasubramanian N. and Wenzel U. (W7-AS Team) 2004 Radiative condensation and detachment in Wendelstein 7-AS stellarator *Nucl. Fusion* **44** 820
[24] Wenzel U., McCormick K., Hildebrandt D., Klose S., Naujoks D. and Thomsen H. 2002 Experimental observation of MARFEs in the W7-AS stellerator *Plasma Phys. Control. Fusion* **44** L57
[25] Peterson B. *et al* 2001 Multifaceted asymmetric radiation from the edge-like asymmetric radiative collapse of density limited plasmas in the large helical device *Phys. Plasmas* **8** 3861–4
[26] Zhang H. *et al* 2017 Vertical profiles and two-dimensional distributions of carbon line emissions from C2+− C5+ ions in attached and RMP-assisted detached plasmas of large helical device *Phys. Plasmas* **24** 022510
[27] Nührenberg J. 2010 Development of quasi-isodynamic stellarators *Plasma Phys. Control. Fusion* **52** 124003
[28] Renner H., Boscary J., Greuner H., Grote H., Hoffmann F.W., Kisslinger J., Strumberger E. and Mendelevitch B. 2002 Divertor concept for the W7-X stellarator and mode of operation *Plasma Phys. Control. Fusion* **44** 1005
[29] Klinger T. *et al* 2019 Overview of first Wendelstein 7-X high-performance operation *Nucl. Fusion* **59** 112004
[30] Wolf R. *et al* 2019 Performance of Wendelstein 7-X stellarator plasmas during the first divertor operation phase *Phys. Plasmas* **26** 082504
[31] Pedersen T.S. *et al* 2019 First divertor physics studies in Wendelstein 7-X *Nucl. Fusion* **59** 096014

[32] Zhang D. *et al* 2019 First observation of a stable highly dissipative divertor plasma regime on the Wendelstein 7-X stellarator *Phys. Rev. Lett.* **123** 025002

[33] Schmitz O. *et al* 2020 Stable heat and particle flux detachment with efficient particle exhaust in the island divertor of Wendelstein 7-X *Nucl. Fusion* **61** 016026

[34] Jakubowski M. *et al* 2021 Overview of the results from divertor experiments with attached and detached plasmas at Wendelstein 7-X and their implications for steady-state operation *Nucl. Fusion* **61** 106003

[35] Zhang D. *et al* 2021 Plasma radiation behavior approaching high-radiation scenarios in W7-X *Nucl. Fusion* **61** 126002

[36] Effenberg F. *et al* 2019 First demonstration of radiative power exhaust with impurity seeding in the island divertor at Wendelstein 7-X *Nucl. Fusion* **59** 106020

[37] Zhang D. *et al* 2010 Design criteria of the bolometer diagnostic for steady-state operation of the W7-X stellarator *Rev. Sci. Instrum.* **81** 10E134

[38] Zhang D. *et al* 2021 Bolometer tomography on Wendelstein 7-X for study of radiation asymmetry *Nucl. Fusion* **61** 116043

[39] Zoletnik S., Biedermann C., Cseh G., Kocsis G., König R., Szabolics T. and Szepesi T. 2018 First results of the multi-purpose real-time processing video camera system on the Wendelstein 7-X stellarator and implications for future devices *Rev. Sci. Instrum.* **89** 013502

[40] Kocsis G. *et al* 2015 Overview video diagnostics for the W7-X stellarator *Fusion Eng. Des.* **96** 808–11

[41] Feng Y. *et al* 1997 A 3D Monte Carlo code for plasma transport in island divertors *J. Nucl. Mater.* **241** 930–4

[42] Feng Y., Sardei F. and Kisslinger J. 1999 3D fluid modelling of the edge plasma by means of a Monte Carlo technique *J. Nucl. Mater.* **266** 812–8

[43] Stangeby P. and Chankin A. 1996 Simple models for the radial and poloidal E× B drifts in the scrape-off layer of a divertor tokamak: effects on in/out asymmetries *Nucl. Fusion* **36** 839

[44] Chankin A. *et al* 1994 The effect of BT reversal on the asymmetries between the strike zones in single null divertor discharges: experiment and theories *Plasma Phys. Control. Fusion* **36** 1853

[45] Chankin A., Corrigan G., Groth M. and Stangeby P.C. 2015 Influence of the E× B drift in high recycling divertors on target asymmetries *Plasma Phys. Control. Fusion* **57** 095002

[46] Feng Y., Herre G., Grigull P. and Sardei F. 1998 The effects of field reversal on the W7-AS island divertor at low densities *Plasma Phys. Control. Fusion* **40** 371

[47] Hammond K. *et al* 2019 Drift effects on W7-X divertor heat and particle fluxes *Plasma Phys. Control. Fusion* **61** 125001

[48] Masuzaki S., Tanaka H., Kobayashi M. and Kawamura G. 2019 Effects of drifts on divertor plasma transport in LHD *Nucl. Mater. Energy* **18** 281–4

[49] Kriete D. *et al* 2023 Effects of drifts on scrape-off layer transport in W7-X *Nucl. Fusion* **63** 026022

[50] Feng Y. 2022 Review of magnetic islands from the divertor perspective and a simplified heat transport model for the island divertor *Plasma Phys. Control. Fusion* **64** 125012

[51] Lazerson S.A. *et al* 2018 Error fields in the Wendelstein 7-X stellarator *Plasma Phys. Control. Fusion* **60** 124002

[52] Bozhenkov S., Otte M., Biedermann C., Jakubowski M., Lazerson S.A., Sunn Pedersen T. and Wolf R.C. 2018 Measurements and correction of the 1/1 error field in Wendelstein 7-X *Nucl. Fusion* **59** 026004

[53] Gao Y. *et al* 2019 Effects of toroidal plasma current on divertor power depositions on Wendelstein 7-X *Nucl. Fusion* **59** 106015

[54] Mast K.F., Vallet J.C., Andelfinger C., Betzler P., Kraus H. and Schramm G. 1991 A low noise highly integrated bolometer array for absolute measurement of VUV and soft x radiation *Rev. Sci. Instrum.* **62** 744–50

[55] Jakubowski M. *et al* 2018 Infrared imaging systems for wall protection in the W7-X stellarator *Rev. Sci. Instrum.* **89** 10E116

[56] Gao Y., Jakubowski M.W., Drewelow P., Pisano F., Puig Sitjes A., Niemann H., Ali A. and Cannas B. 2019 Methods for quantitative study of divertor heat loads on W7-X *Nucl. Fusion* **59** 066007

[57] Feng Y. *et al* 2021 First attempt to quantify W7-X island divertor plasma by local experiment-model comparison *Nucl. Fusion* **61** 106018

[58] Kremeyer T. *et al* 2022 Analysis of hydrogen fueling, recycling, and confinement at Wendelstein 7-X via a single-reservoir particle balance *Nucl. Fusion* **62** 036023

[59] Rudischhauser L., Endler M., Höfel U., Hammond K.C., Kallmeyer J.P. and Blackwell B.D. 2020 The Langmuir probe system in the Wendelstein 7-X test divertor *Rev. Sci. Instrum.* **91** 063505

[60] Haak V., Bozhenkov S.A., Feng Y., Kharwandikar A., Kremeyer T., Naujoks D., Perseo V., Schlisio G. and Wenzel U. 2023 Overview over the neutral gas pressures in Wendelstein 7-X during divertor operation under boronized wall conditions *Plasma Phys. Control. Fusion* **65** 055024

[61] Wenzel U., Schlisio G., Mulsow M., Pedersen T.S., Singer M., Marquardt M., Pilopp D. and Rüter N. 2019 Performance of new crystal cathode pressure gauges for long-pulse operation in the Wendelstein 7-X stellarator *Rev. Sci. Instrum.* **90** 123507

[62] Schlisio G. *et al* 2021 The evolution of the bound particle reservoir in Wendelstein 7-X and its influence on plasma control *Nucl. Fusion* **61** 036031

[63] Pasch E., Beurskens M.N.A., Bozhenkov S.A., Fuchert G., Knauer J. and Wolf R.C. 2016 The Thomson scattering system at Wendelstein 7-X *Rev. Sci. Instrum.* **87** 11E729

[64] Bozhenkov S.A. *et al* 2017 The Thomson scattering diagnostic at Wendelstein 7-X and its performance in the first operation phase *J. Instrum.* **12** P10004

[65] Knauer J. *et al* 2016 A new dispersion interferometer for the stellarator Wendelstein 7-X *43rd EPS Conf. on Plasma Physics* (*Leuven, Belgium, 4–8 July 2016*) (European Physical Society) (available at: https://kuleuvencongres.be/eps2016)

[66] Rahbarnia K. *et al* 2018 Diamagnetic energy measurement during the first operational phase at the Wendelstein 7-X stellarator *Nucl. Fusion* **58** 096010

[67] Pavone A. *et al* 2019 Measurements of visible bremsstrahlung and automatic Bayesian inference of the effective plasma charge Zeff at W7-X *J. Instrum.* **14** C10003

[68] Feng Y., Reiter D. and Frerichs H. 2025 A novel method for treating MAR in EMC3-Eirene, and first applications to W7-X *Nucl. Fusion* **65** 066008

[69] Zhang D. *et al* 2023 Observation of impurity accumulation and its compatibility with high plasma performance in W7-X *Plasma Phys. Control. Fusion* **65** 105006

[70] Rasmussen C.E. and Williams C. 2006 *Gaussian Processes for Machine Learning* vol 32 (The Mit Press) p 68

[71] Krychowiak M. *et al* 2021 Gaussian Process Tomography of carbon radiation in the transition to detached plasmas in the Wendelstein 7-X stellarator *47th EPS Conf. on Plasma Physics* (*Sitges, Spain, 21–25 June 2021*) (European Physical Society) (available at: https://epsplasma2020.eu/)

[72] Feng Y. *et al* 2024 Conditions and benefits of X-point radiation for the island divertor *Nucl. Fusion* **64** 086027

[73] Hirsch M. *et al* 2019 ECE diagnostic for the initial operation of Wendelstein 7-X *EPJ Web of Conf.* vol 203 p 03007 (EDP Sciences)

[74] Winters V. *et al* 2024 Impurity leakage mechanisms in the Wendelstein 7-X island divertor under friction-dominated conditions *Nucl. Fusion* **64** 056042
[75] Kawamura G., Feng Y., Kobayashi M., Shoji M., Morisaki T., Masuzaki S. and Tomita Y. 2014 First EMC3-EIRENE simulations with divertor legs of LHD in realistic device geometry *Contrib. Plasma Phys.* **54** 437–41
[76] Summers H. and McWhirter R. 1979 Radiative power loss from laboratory and astrophysical plasmas. I. Power loss from plasmas in steady-state ionisation balance *J. Phys. B: At. Mol. Phys.* **12** 2387
[77] Perseo V. *et al* 2021 2D measurements of parallel counter-streaming flows in the W7-X scrape-off layer for attached and detached plasmas *Nucl. Fusion* **61** 116039
[78] Killer C., Grulke O., Drews P., Gao Y., Jakubowski M., Knieps A., Nicolai D., Niemann H., Sitjes A.P. and Satheeswaran G. 2019 Characterization of the W7-X scrape-off layer using reciprocating probes *Nucl. Fusion* **59** 086013
[79] Krämer-Flecken A. *et al* 2019 Investigation of turbulence rotation and radial electric field in the island divertor and plasma edge at W7-X *Plasma Phys. Control. Fusion* **61** 054003